UC Riverside

UC Riverside Electronic Theses and Dissertations

Title

A Novel Combination of Non-Thermal Plasma Synthesis and Spark Plasma Sintering for the Creation of Non-Equilibrium Materials

Permalink

https://escholarship.org/uc/item/30q1j8r9

Author

Herzberg, Steven Andrew

Publication Date

2024

Copyright Information

This work is made available under the terms of a Creative Commons Attribution License, available at https://creativecommons.org/licenses/by/4.0/

Peer reviewed|Thesis/dissertation

eScholarship.org Powered by the California Digital Library
University of California

UNIVERSITY OF CALIFORNIA
RIVERSIDE

A Novel Combination of Non-Thermal Plasma Synthesis and Spark Plasma Sintering for the Creation of Non-Equilibrium Materials

A Dissertation submitted in partial satisfaction
of the requirements for the degree of

Doctor of Philosophy

in

Mechanical Engineering

by

Steven Herzberg

June 2024

Dissertation Committee:
Prof. Lorenzo Mangolini, Co-Chairperson
Prof. Suveen Mathaudhu, Co-Chairperson
Prof. Chen Li

Copyrighted by
Steven Herzberg
2024

The Dissertation of Steven Herzberg is approved:

_____

_____

_____

Committee Chairperson

University of California, Riverside

Acknowledgements

Firstly, I would like to express my gratitude towards my co-advisors Dr. Lorenzo Mangolini and Dr. Suveen Mathaudhu for their guidance, support, and patience with me throughout my time at UCR.

I would also like to thank the members of my Dissertation/Qualifying Committees for their constructive feedback.

I acknowledge previously published work has been reprinted or partially reprinted from the journal **Plasma Processes and Polymers**, volume 20, May 2023 (Chapter 1). I am the primary contributor to this article, while Dr. Suveen Mathaudhu and Dr. Lorenzo Mangolini are contributors. For this particular work I also acknowledge the UCR Center for Advanced Microscopy and Microanalysis (CFAMM) and UCR Materials Science and Engineering for the use of their facilities, in particular Dr. Krassimir Bozhilov, who performed TEM/EDS and SAED measurements for my research. As well as Dr. Ilkeun Lee for performing XPS measurements for my research.

I also acknowledge work submitted to UCR's eScholarship repository has been reprinted or partially reprinted. I am the primary contributor while Joshua Edwards, Dr. Alexander Dupuy, Dr. Lorenzo Mangolini, and Dr. Suveen Mathaudhu are contributors. Additional individuals are acknowledged for their contributions in other areas of my research including Eric Eyerman and Brandon To from CalNano for performing high-pressure/high-temperature SPS.

I acknowledge the support of the Department of Education Graduate Assistance in Areas of National Need (GAANN) for funding my research.

ABSTRACT OF THE DISSERTATION

A Novel Combination of Non-Thermal Plasma Synthesis and Spark Plasma Sintering for the Creation of Non-Equilibrium Materials

by

Steven Herzberg

Doctor of Philosophy, Graduate Program in Mechanical Engineering
University of California, Riverside, June 2024
Prof. Lorenzo Mangolini and Prof. Suveen Mathaudhu, Co-Chairpersons

The growing interest in non-equilibrium processing over the past few decades has led to numerous published works. A few examples of these techniques include rapid solidification, age hardening, mechanical alloying, and severe plastic deformation. This has also led to the creation of new types of materials such as bulk metallic glasses and nanomaterials. This work presents a novel approach for producing non-equilibrium materials in bulk form through a combination of Non-Thermal Plasma (NTP) synthesis and Spark Plasma Sintering (SPS). First, amorphous silicon carbonitride nanoparticles are produced non-thermal plasma synthesis from a combination for gaseous precursors including silane (SiH_4), methane (CH_4), and ammonia (NH_3). A combination of high temperature baking experiments followed by X-Ray Diffraction (XRD), show that the plasma synthesized SiCN can maintain an amorphous phase up to 2000 °C, whereas literature reports a typical crystallization temperature ranging from 1400 °C-1600 °C. However, porosity of these samples remained high, severely impacting mechanical properties, due to N_2 outgassing occurring at 1450 °C. A follow up experiment was

conducted to consolidate SiCN nanoparticles into a dense, bulk material via SPS with varying degrees of devitrification and segregation of the SiCN into a composite of crystalline SiC/Si_3N_4. With a custom high temperature, high pressure tooling consisting of SiC punches graphite dies, achieving a density of 3.21 g/cm^3. Mechanical testing of the sintered SiCN shows a maximum Vickers hardness of 16.1 GPa, fracture toughness of 2.6 $MPa \cdot m^{1/2}$, and Young's Modulus of 247 GPa, placing these samples well within the margin of those reported on in literature. Post-sintering analysis shows that the presence of β-SiC nanocrystals after sintering of both samples, with the one sintered at 1600 °C also containing α-Si_3N_4 and β-Si_3N_4.

Table of Contents

Table of Figures

List of Tables

Chapter 1. Background

1.1 Non-Equilibrium Processing

Materials produced under non-equilibrium conditions have been used by humanity for hundreds of years, but only in the past century have we started to understand the mechanisms that create such materials. Non-equilibrium materials are materials that exist in states which, according to thermodynamics, they should not be in. The reason a non-equilibrium phase can exist is due to kinetics (*i. e.* atomic diffusion). As a material cools from one phase to the next, if the cooling is fast enough, the atoms can "freeze" in place regardless of if they formed their equilibrium phase or not. Ishihara gives an example of this concept using a hypothetical polymorphic material with α as its equilibrium solid phase, based off of its free energy, with β, γ, and δ being metastable solid phases at all temperatures (Figure 1.1a).[1] In this scenario, increasing temperature past T_m^{α} results in the liquid phase becoming the most stable phase. Once the liquid phase has formed, if temperature is decreased back down to less than T_m^{α}, but higher than T_m^{β}, the liquid will begin to convert back to α. Given enough time, the liquid phase will completely convert to α, which is the most stable phase. However, if temperature is lowered below T_m^{β}, and sufficient time is not given for the liquid phase to completely convert to α, the liquid will start to form the β phase. The α phase can still form in these conditions, and given enough time the β phase can completely convert to α. This is based off the Ostwald Step Rule, which elucidates that when there are multiple polymorphs a phase can transition to, it is not the most stable (*i. e.* lowest energy) phase that forms. Instead, the phase which is closest in energy to the current phase will form, even if the

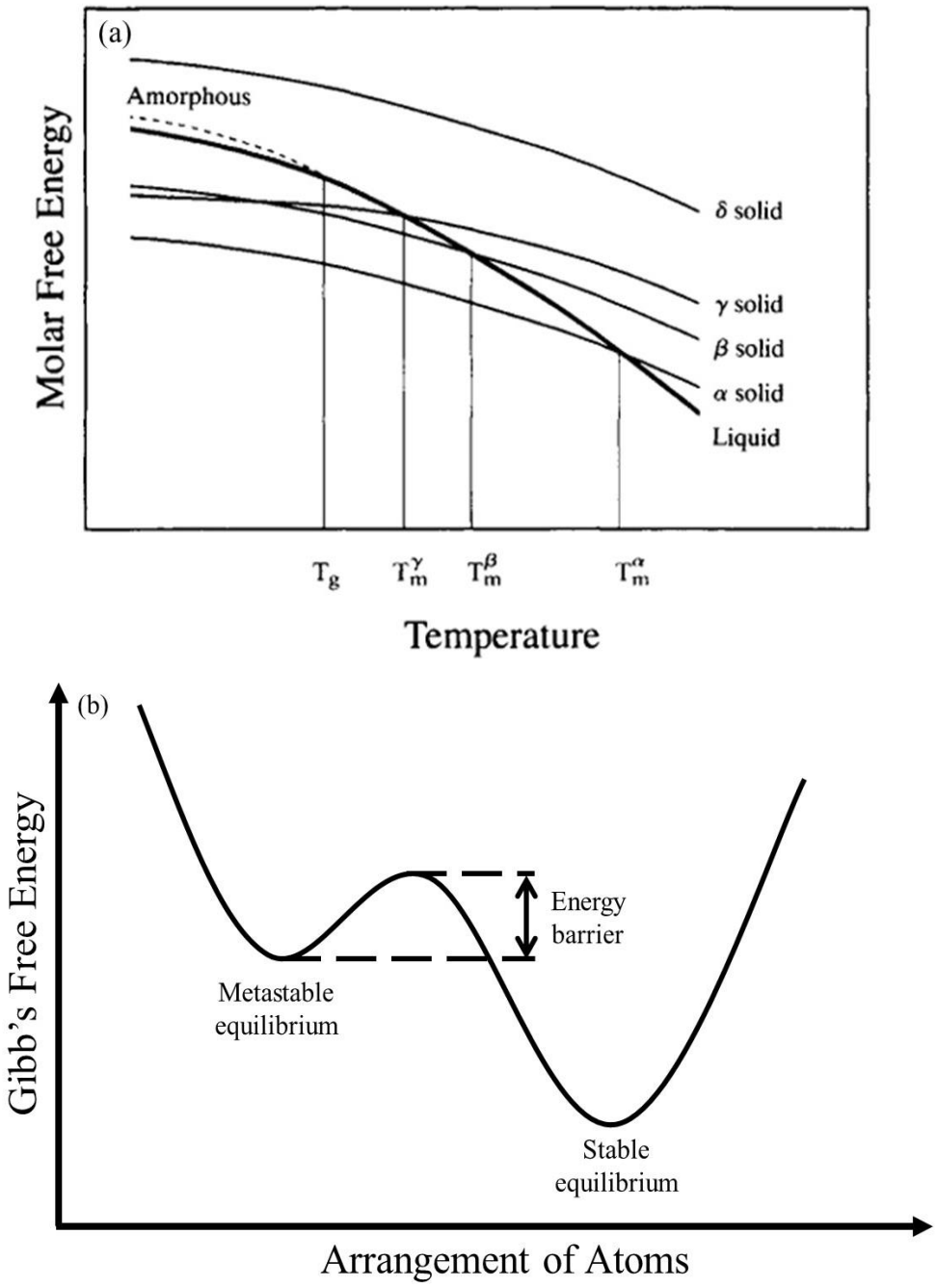

Figure 1.1 (a) Free energy vs. temperature plot of a hypothetical element with metastable phases [1] (b) Free energy vs atomic arrangement of a hypothetical element in a metastable state.

next phase is not the most stable.[2] Similarly, rapid cooling of the liquid below T_m^{γ} can form the γ, β, and α phases. It should be noted that the δ phase cannot be formed from liquid as its free energy is never lower than that of the liquid phase, instead the δ phase would have to form from the vapor phase. The last possible phase to form from any undercooled liquid would be the amorphous (or glass) phase indicated by T_g (glass transition temperature), where its solidus line is represented at the dotted line in Figure 1.1a. The amorphous phase is a non-crystalline phase where the atomic arrangement originates from the disordered arrangement of the liquid, but frozen in place. With further cooling, the low thermal energy in the material eventually becomes insufficient to drive atomic diffusion. From this point, any β, γ, δ, and amorphous phases will persist in metastable equilibrium, as opposed to transitioning to a lower energy stable equilibrium. What's known as an activation barrier now exists between the metastable and stable states (Figure 1.1b). To reach the stable phase from a metastable state, an activation energy must be input into the system to reengage atomic diffusion for transitioning to a lower energy state.

In the real world, metastable materials exist within nature and humans have been making them for thousands of years. Pottery, which is clay that has been heated in a fire to become rigid, requires a glassy coating (known as glaze) for impermeability. The use of glazing dates back to 1500 BCE Egypt,[3] but amorphous phases have been found within artifacts dated as far back as 6000 BCE.[4] With the histories of metallurgy, blacksmiths would quench steel tools and weapons to harden them. Martensitic steel has been found in ancient tools dating 100-200 CE.[5] One of the first major breakthroughs

in our understanding of non-equilibrium processing began with the study of age hardening. Age hardening is the heating of a supersaturated alloy at low temperatures leading to the formation of metastable precipitates within the alloy matrix.[6] These precipitates harden the alloy by impeding the movement of dislocations. Age hardening was first discovered in 1906 by Alfred Wilm with an Al-Cu-Mg alloy called Duralumin.[7] However, it was not until 1919 when P. D. Merica *et al.* that deduced $CuAl_2$ particles were precipitating out of the solid solution.[8] Since the works of Wilm and Merica, age hardened materials have become integral in areas such as the aerospace where aged hardened Al and Ti alloys provide the necessary strength-to-weight ratio for airplanes and rockets.[9,10] To this day new non-equilibrium processing methods have continued to develop and have led to the creation of new materials, in addition to modifying existing ones.

Rapid solidification which uses cools liquids into solids at a rates higher than 10^4 K/s to form a variety of supersaturated, amorphous, and metastable crystalline materials.[11] Rapid solidification can be undertaken with different techniques to make products in different forms. Atomization where a molten metal alloy is passed into a high velocity fluid stream, atomizing the melt in fine droplets and solidifying the droplets in micron sized particles. Continuous casting involves molten metals being deposited onto chilled, rapid (linear or rotating) moving substrates forming ribbons, foils, or wires. and laser processing results in the formation of powders, ribbons/foils/filaments, and surface modified billets, respectively. Spraying forming techniques are a combination of

atomization and casting where the semi-molten droplets are deposited onto substrates for the near-net production of films or parts.

Rapid solidification casting techniques have been used to create new non-equilibrium materials such as metallic glasses (amorphous metal alloys).[12,13] The inclusion of large ratios of alloying elements has reduced the required quenching rates to prevent crystal nucleation. In doing so, the lower quenching rates allowed for thinker foils of larger metallic glasses to be made, now designated as bulk metallic glasses (BMGs).[14] These BMGs display good wear resistance[15] and corrosion resistance[16] in comparison to their crystalline, equilibrium forms. BMGs also display super elasticity while having almost no plasticity due to their complete lack of slip planes.

Mechanical alloying (MA) is used for the mixing of dissimilar materials. This is undertaken through high energy ball milling, where feedstock powders are placed within a hardened steel, WC, or Al_2O_3 jar, along with balls made of the same materials, and everything is violently shaken together. The balls crush and grind the particles together, with the initial period of milling consisting of deforming and cold welding of the particles together. As the particles work harden, they eventually become brittle and fracture into smaller particles. From this point, the particle fractures cold weld together again, fracture again, and repeat, meanwhile if the different powders are mixing. To harder of the materials typically embeds onto the surface of the softer as the particles are crushed together by the milling media. As the softer particle fractures and rewelds together, the harder particle ends up inside the newly welded agglomeration, becoming more dispersed with the softer material as more fractures and rewelds occur. This goes on until a steady

state particle size and mixture is reached.[17] The novelty of MA is that this mixing method has the capability to force materials into a solid solution through this fracture-reweld process. This is useful for forming alloys out of metals with a wide difference in melting points that would normally prevent them from forming and staying in solution during a melt and solidification. This can also include the mixing of metals and ceramics to form metal matrix composites.[18] In addition, the constant cold working refines the grains and can lead to amorphization.[19]

Ultrafine-grained (UFG) materials are another class of non-equilibrium materials driving research into new processing techniques. UFG materials, or nanograined materials, contain grains <100 nm in size. UFGs can result in a significant increase in mechanical properties in comparison to coarse grains. For instance, the Hall-Petch relationship shows that reducing grain size increases strength.[20] The UFGs also exhibit superplasticity due to the prevalence of grain boundary sliding and intragranular flow.[21] The production of UFGs is typically achieved through severe plastic deformation methods such as high-pressure torsion or equal channel angular pressing to reduce the size of larger grains into nanosized grains.[22]

1.2 Non-Thermal Plasma Synthesis

Plasma synthesis has been used to create non-equilibrium ceramic and metal powders and thin films through the highly reactive environment of free radicals.[23] There are two types of plasmas which can be used: thermal or non-thermal. Thermal plasma synthesis is a type of rapid solidification technique that can be used for atomization or spray forming. Thermal plasma synthesis involves the vaporization of

materials at high temperatures, with the now gaseous materials being deposited onto substrates to form a film or condense into solid particles.[24,25] An important process within thermal plasmas that make them unique among other rapid solidification techniques is that the high temperatures (>10^4 K) leads to the formation of highly reaction ion radicals. This can be useful for creating new compounds either on the surface of a substrate or with other vaporized materials. Of note, the highly reactive gaseous environment of plasmas also allows for the creation of ceramics by mixing in gasses such as O_2, N_2, and CH_4.[25–27] Additionally, the since particles are nucleated from a gaseous phase and quenched upon exiting the plasma, it is possible to make nanoparticles.[26]

Non-thermal plasmas achieve this feat through the application of an alternating E-field that pushes and pulls free electrons back and forth. With enough power applied to the system, the electrons can reach velocities that can break free a valence electron from a precursor compound upon collision, ionizing the compound. As more free electrons collide with neutral species, the number of electrons grows exponentially. Eventually there is an avalanche of free electrons leading to the generation of the plasma. While ionization events are occurring in the plasma, so are recombination events. Where electrons collide with and are absorbed into ions converting them back to a neutral species. The balance of ionization and recombination events at equal rates keeps the number of ions and electrons roughly equal and the plasma stable (Figure 1.2). Due to the large difference in mass between electrons and ions, the electrons have significantly higher thermal velocities than the ions. As a result, non-thermal plasmas are not at thermal equilibrium, unlike thermal plasmas.[23] The far from thermal equilibrium nature

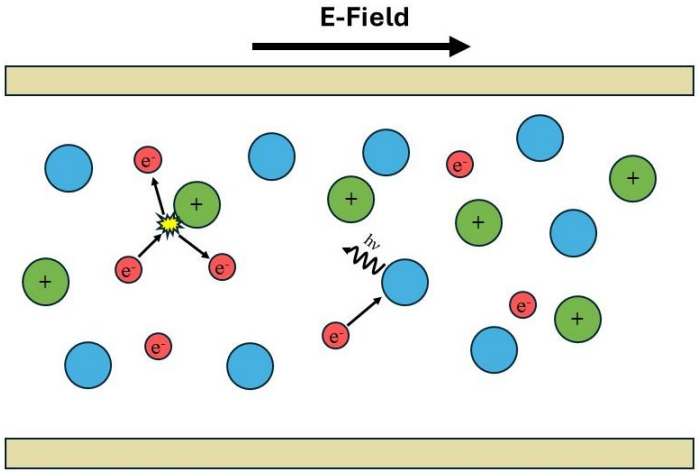

Figure 1.2 Diagram of a non-thermal plasma displaying an ionization and a recombination event.

of non-thermal plasma synthesis leads to several novel mechanisms occurring during and after particle formation. A relatively low temperature for the gas allows the forming particles to maintain an amorphous state. But crystallization can still occur as ions deposit onto particles and release energy in the form of heat. If enough ions deposit a short enough time frame, the cumulative heat can drive crystallization of the particle. [28,29] Additionally, the electrons, which are moving significantly faster than everything else, are constantly bombarding the forming particles, negatively charging them. The negatively charged particles start to repel each other leading to particle growth through agglomeration to be greatly reduced.[30] The primary mode of particle growth is instead through ion deposition.[31] As a result, the final particle size distribution is narrow with a possible average particle size being less than 10 nanometers.

Originally non-thermal plasmas were used to break down silane (SiH_4) and make silicon.[32,33] Since then, it has been used to make several types of silicon compounds through the addition of other precursors such as silicon carbide from methane,[34] silicon nitride from ammonia.[35] Additionally, there have been studies on the viability to

produce silicon quantum dots from non-thermal plasmas.[36] It has also been used to create plasmonic materials such as titanium nitride nanoparticles.[37] With growing interest in ammonia for clean hydrogen storage, non-thermal plasma synthesis has been shown to be viable for ammonia catalysis.[38] Non-thermal plasma has also been used to form metal nanoparticles such as aluminum and nickel.[39,40] The caveat is that most of these studies have either been exploratory on the viability of non-thermal plasma synthesis for producing these materials, or in regard to the electrical or optical properties of such materials. Little work has investigated what structural properties plasma synthesized materials may have even as many of these studies involve structural ceramics such as SiC and TiN. To effectively study the structural properties, these materials would first need to be transformed from powder to bulk in a process known as sintering.

1.3 Spark Plasma Sintering

Sintering is the process of using heat and/or pressure on a powder to consolidate it into bulk form without melting it.[41] Typically sintering occurs at the glass transition temperature of a given material as that is when the material can become highly plastic. Sintering occurs in stages with the first simply being loose particle in contact with each other and sintering having not yet begun (Figure 1.3a). The initial stage of sintering is defined by neck formation at the interface of particles (Figure 1.3b). The formation of necks is driven by evaporation-condensation of the between the surfaces of the particles. The intermediate stage involves the growth of necks formed during the initial stage, but an open pore network is still present (Figure 1.3c). Surface energy drives diffusion to reduce the surface area. The final stage begins when most of the open pores from the

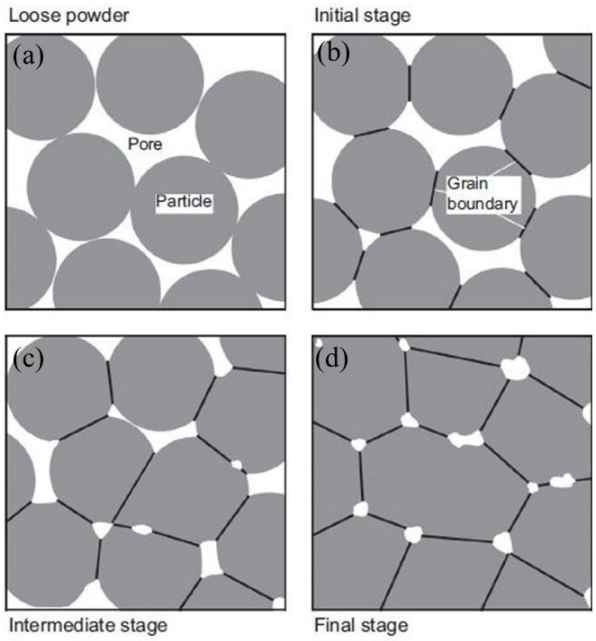

Figure 1.3 Stages of sintering (a) loose powder before sintering has begun (b) initial stage where necks begin to for (c) intermediate stage defined by neck growth (d) final stage of sintering where grain boundary diffusion of pores drives densification.[41]

intermediate stage close (Figure 1.3d). From this point, diffusion is driven by grain boundary energy (reducing the size of grain boundaries by coarsening the grains). The closed pores travel along the grain boundaries out of the materials. Stress is applied to the pores as the grains shift and rotate.

In order to maintain amorphous or nanostructured phases when sintering powders into bulk form, sintering time must be as short as possible to reduce grain coarsening.[42] Spark plasma sintering (SPS), also known as Field Assisted Sintering Technique (FAST), is commonly used for densification of non-equilibrium powders into bulk form. SPS differs from conventional sintering by using a conductive graphite punch+die set to hold the feedstock powder and applying a pulsed direct current through the die set and material (if conductive). The current passing through the die set generates heat through Joule heating. This creates much higher heating rates up to 1000°C/min[43] as the

material (or at least the die) is heated directly. In comparison, conventional heating methods with furnaces usually have a heating rate around 10°C/min. Additionally, cooling rates are usually 150°C/min, but can be further increased up to 400°C/min by quenching the die with nonreactive flowing gases. Higher heating and cooling rates lead to shorter sintering times, which in turn reduces grain coarsening and preservation of the original microstructure present in the feedstock. A uniaxial pressure is applied to the punch+die set during sintering to This has been important when working with non-equilibrium powders and converting them to bulk without the annihilation of the non-equilibrium phase.[44,45] Additionally, there is some evidence that the presence of an E-field on the feedstock during sintering can enhance densification.[46]

1.4 Objectives

By combining non-thermal plasma synthesis with SPS, we hope to develop a novel approach for producing non-equilibrium materials in bulk form. As mentioned prior, non-thermal plasma synthesis is primarily used to create films and powders; few reports address the viability of sintering such powders and what properties they might have. Our approach will tackle two questions: Can non-thermal plasma synthesis create compounds more complex than binary compounds? What are the structural properties of plasma synthesized materials, and do they differ from other methods?

1.5 Citations

[1] K. N. Ishihara, in *Non-Equilibrium Processing of Materials* (Ed.: C. Suryanarayana), Amsterdam; New York: Pergamon, **1999**, pp. 5–20.

[2] W. Ostwald, *Zeitschrift für Physikalische Chemie* **1897**, *22U*, 289.

[3] P. Colomban, in *Conservation Science: Heritage Materials, 2nd Edition, P. Garside & E. Richardson Eds, RSC*, **2020**.

[4] M. S. Tite, Y. Maniatis, *Nature* **1975**, *257*, 122.

[5] J. Lang, *Materials and Manufacturing Processes* **2017**, *32*, 857.

[6] C. Sigli, F. D. Geuser, A. Deschamps, J. Lépinoux, M. Perez, *Comptes Rendus. Physique* **2018**, *19*, 688.

[7] A. Wilm, *Metallurgie* **1911**, *8*, 225.

[8] P. D. Merica, R. G. Waltenberg, H. Scott, *Sci. Pap. Bur. Stand.* **1919**, *15*, 271.

[9] M. Nakai, T. Eto, *Materials Science and Engineering: A* **2000**, *285*, 62.

[10] S. A. Mantri, D. Choudhuri, T. Alam, G. B. Viswanathan, J. M. Sosa, H. L. Fraser, R. Banerjee, *Scripta Materialia* **2018**, *154*, 139.

[11] E. J. Lavernia, T. S. Srivatsan, *J Mater Sci* **2010**, *45*, 287.

[12] P. Duwez, R. H. Willens, W. Klement, *Journal of Applied Physics* **1960**, *31*, 1136.

[13] W. Klement, R. H. Willens, P. Duwez, *Nature* **1960**, *187*, 869.

[14] W. H. Wang, C. Dong, C. H. Shek, *Materials Science and Engineering: R: Reports* **2004**, *44*, 45.

[15] A. L. Greer, K. L. Rutherford, I. M. Hutchings, *International Materials Reviews* **2002**, *47*, 87.

[16] S. J. Pang, T. Zhang, K. Asami, A. Inoue, *Acta Materialia* **2002**, *50*, 489.

[17] C. Suryanarayana, *Progress in Materials Science* **2001**, *46*, 1.

[18] L. Lu, M. O. Lai, C. W. Ng, *Materials Science and Engineering: A* **1998**, *252*, 203.

[19] C. C. Koch, *Journal of Non-Crystalline Solids* **1990**, *117–118*, 670.

[20] N. Hansen, *Scripta Materialia* **2004**, *51*, 801.

[21] M. Kawasaki, T. G. Langdon, *J Mater Sci* **2007**, *42*, 1782.

[22] S. M. Ghalehbandi, M. Malaki, M. Gupta, *Applied Sciences* **2019**, *9*, 3627.

[23] U. R. Kortshagen, R. M. Sankaran, R. N. Pereira, S. L. Girshick, J. J. Wu, E. S. Aydil, *Chem. Rev.* **2016**, *116*, 11061.

[24] S. Sampath, H. Herman, *JTST* **1996**, *5*, 445.

[25] P. Ronsheim, A. Mazza, A. N. Christensen, *Plasma Chem Plasma Process* **1981**, *1*, 135.

[26] J.-H. Seo, B.-G. Hong, *Nuclear Engineering and Technology* **2012**, *44*, 9.

[27] S. Samal, *Journal of Cleaner Production* **2017**, *142*, 3131.

[28] N. J. Kramer, R. J. Anthony, M. Mamunuru, E. S. Aydil, U. R. Kortshagen, *J. Phys. D: Appl. Phys.* **2014**, *47*, 075202.

[29] T. Lopez, L. Mangolini, *Nanoscale* **2014**, *6*, 1286.

[30] J. Goree, *Plasma Sources Sci. Technol.* **1994**, *3*, 400.

[31] L. Mangolini, *Journal of Vacuum Science & Technology B* **2013**, *31*, 020801.

[32] M. K. Alam, R. C. Flagan, *Aerosol Science and Technology* **1986**, *5*, 237.

[33] A. Bouchoule, A. Plain, L. Boufendi, J. Ph. Blondeau, C. Laure, *Journal of Applied Physics* **1991**, *70*, 1991.

[34] D. Coleman, L. Mangolini, *ACS Omega* **2019**, *4*, 10089.

[35] J. Szépvölgyi, I. Mohai-Tóth, *Journal of Materials Chemistry* **1995**, *5*, 1227.

[36] J. Schwan, K. Wang, M. Lee Tang, L. Mangolini, *Nanoscale* **2022**, *14*, 17385.

[37] A. Alvarez Barragan, N. V. Ilawe, L. Zhong, B. M. Wong, L. Mangolini, *J. Phys. Chem. C* **2017**, *121*, 2316.

[38] D. Zhou, R. Zhou, R. Zhou, B. Liu, T. Zhang, Y. Xian, P. J. Cullen, X. Lu, K. (Ken) Ostrikov, *Chemical Engineering Journal* **2021**, *421*, 129544.

[39] A. Woodard, L. Xu, A. A. Barragan, G. Nava, B. M. Wong, L. Mangolini, *Plasma Processes and Polymers* **2018**, *15*, 1700104.

[40] C. A. Beaudette, H. P. Andaraarachchi, C.-C. Wu, U. R. Kortshagen, *Nanotechnology* **2021**, DOI 10.1088/1361-6528/ac0cb3.

[41] R. German, *Sintering: From Empirical Observations to Scientific Principles*, Butterworth-Heinemann, **2014**.

[42] Z. Z. Fang, H. Wang, V. Kumar, *International Journal of Refractory Metals and Hard Materials* **2017**, *62*, 110.

[43] O. Guillon, J. Gonzalez-Julian, B. Dargatz, T. Kessel, G. Schierning, J. Räthel, M. Herrmann, *Adv. Eng. Mater.* **2014**, *16*, 830.

[44] Y. Long, H. Zhang, T. Wang, X. Huang, Y. Li, J. Wu, H. Chen, *Materials Science and Engineering: A* **2013**, *585*, 408.

[45] T. Grosdidier, G. Ji, F. Bernard, E. Gaffet, Z. A. Munir, S. Launois, *Intermetallics* **2006**, *14*, 1208.

[46] S. Grasso, Y. Sakka, *Journal of the Ceramic Society of Japan* **2013**, *121*, 524.

Chapter 2. Non-Thermal Plasma Synthesis of Silicon Carbonitride

2.1 Abstract

The use of a low-temperature plasma for the synthesis of amorphous silicon carbonitride nanoparticles enables the realization of sintered bulk samples with high thermal stability. Amorphous SiCN is produced from a mixture of silane, methane and ammonia and utilizing a mid-pressure, radio-frequency, continuous flow reactor. Particle characterization shows the nanoparticles are largely amorphous with some crystalline silicon carbide domains <10 nm in size. Compositional tuning, controlled through variable precursor flow rates, coupled with the uniform mixing of elements at the nanoscale, results in samples that resist crystallization even when sintered at temperatures up to 2000°C. This study suggests that the low-temperature plasma synthesis of nanoparticles has great potential to produce bulk structural materials for application in harsh environments.

2.2 Introduction

Low-temperature, non-thermal plasma synthesis is a versatile method for the generation of nanoparticles. Among the benefits of these processes is the capability of generating small particles with a narrow size distribution, an inherent consequence of the non-thermal equilibrium between free electrons and other species which results in the unipolar charging of particles.[1–3] While these processes have been initially investigated for the case of silicon and carbon nanoparticles, in recent years there has been a multitude of reports focusing on more complex chemistries, such as nitrides[4–6] and carbides.[7–9] In addition, these processes allow for the production of particles locked in a non-

equilibrium phase, i.e. particles with glassy or amorphous structure. This can be easily achieved by varying parameters such as electrical power input, lowering it to the point in which sufficient plasma density is achieved to activate the chemical precursor and drive the nucleation of particles, but not sufficient to drive their crystallization.[10,11] To our knowledge, the deliberate formation of amorphous particles is difficult to achieve in other processes that typically rely on high temperatures, such as laser pyrolysis, flame synthesis, or thermal plasma synthesis.

Because of these advantageous properties, nanoparticles produced via non-thermal plasma are being explored for a broad range of applications. Ultra-small silicon particles, or quantum dots, have interesting optical properties for electronics and bio-related applications.[12–14] Silicon carbide particles can be used as electron-scattering inclusions in silicon-based thermoelectric devices, improving their efficiency.[15] Titanium and zirconium nitride particles are a low-cost alternative to gold- and silver-based plasmonic materials.[16,17] Finally, amorphous silicon particles have recently been shown to have energetic characteristics that are superior to their crystalline counterpart.[10]

In this manuscript, we describe the synthesis and characterization of ternary amorphous particles composed of silicon, carbon and nitrogen (SiCN). Silicon carbonitride (SiCN) is of great interest for application in high temperature, chemically harsh environments. This is due to SiCN's good oxidation resistance[18] and creep hardening[19] at high temperatures, which are the key features in potential materials for turbine blades and heat shielding for aerospace applications.[20,21] SiCN has primarily

been made through the liquid phase method of pyrolysis of polymer precursors. This method involves the use of organosilicon polymers such as polysilazanes or polysilylcarbodiimides,[22,23] which are cross-linked and shaped before undergoing ceramization via pyrolysis at 1100 °C.[24] During pyrolysis, volatile byproducts outgas from the SiCN resulting in a porous bulk body. A post-processing technique for increasing the density involves pulverizing (via ball milling) the SiCN into powder form and then sintering the powder into a bulk sample.[25] One of the primary advantages of gas-phase over liquid-phase particle synthesis methods, is that liquid-phase requires additional effort to remove byproducts, whereas gas-phase byproducts are mostly gaseous making it easier to produce contaminant-free powders.[26] Another approach for SiCN nanoparticle generation is laser pyrolysis of aerosolized liquid precursors to form nanoparticles.[27] Both methods come with some detrimental aspects - the ball milling has limited particle refinement and introduces contaminants,[28] while the nanoparticles formed in laser pyrolysis are prone to agglomeration.[29] Both methods therefore present challenges. In addition, the sintering of SiCN is non-trivial. SiCN undergoes crystallization at approximately 1500 °C, accompanied by segregation into a SiC/Si_3N_4 composite,[20] leaving only a few studies on the mechanical properties of true bulk SiCN as opposed to the composite structure.

Motivated by these considerations, we explore an alternative approach to the synthesis of feedstock SiCN powders with the goal of investigating the thermal stability of bulk SiCN samples. We choose low-temperature, non-thermal plasma as the synthetic process for SiCN nanoparticles because of the advantageous properties outlined

previously in this introduction. In particular, in this report we show that amorphous SiCN nanoparticles with controllable composition can be produced using a mixture of silane, methane and ammonia as precursors. Preliminary studies on the sintering of these particles indeed confirm that highly stable bulk, amorphous SiCN can be achieved even when sintering at temperatures as high as 2000 °C. This compares favorably to the case of SiCN powders from liquid-phase synthesis, which crystallize in the 1400 - 1700 °C range depending on composition.[23] The tunability of composition is an important characteristic, as we have found that crystallization onset strongly varies even with minor variations in the Si:C:N ratios. Overall, this study provides yet another confirmation that low-temperature plasma processes can produce particles with improved and desirable behavior compared to more broadly utilized synthetic approaches.

2.3 Materials and Methods

The SiCN nanoparticles were produced with an Ar-SiH_4 mixture (1.37% SiH_4), CH_4, and NH_3 were used as gaseous precursors. As shown in Figure 2.1, the precursor gases are passed through an Al_2O_3 tube reactor at a pressure of 3 torr. A continuous capacitively coupled non-thermal plasma was generated in the Al_2O_3 reactor with a copper ring electrode using a radio frequency (RF) power source (13.56 MHz). The nanoparticles formed in the plasma were immediately passed through a quartz reactor placed in a tube furnace (OTF-1200X, MTI Corporation, CA, USA) set to 1000 °C to perform an in-flight annealing and remove any excess hydrogen from the nanoparticles.[30] The in-flight de-hydrogenation (annealing) step has no significant effect on the amorphous structure of the SiCN nanoparticles. Based on our experience,

the in-flight annealing step is crucial since the presence of hydrogen makes it impossible to achieve a solid sample after sintering, because of hydrogen-induced embrittlement, as shown in Figure 2.2. The nanoparticles were collected on a stainless-steel mesh filter which is then pressurized to atmospheric pressure with argon and sealed. The filter with the nanoparticles was transferred into a glovebox where the nanoparticles were removed from the filter. The power for the plasma was initially varied from 50-120 W in steps of 10 W. A power of 100 W produced the most SiCN without major in-situ crystallization and was used for the following runs. Using said power for production of amorphous nanoparticles, the flow rates of the gaseous precursors were varied as shown in Table 2.1.

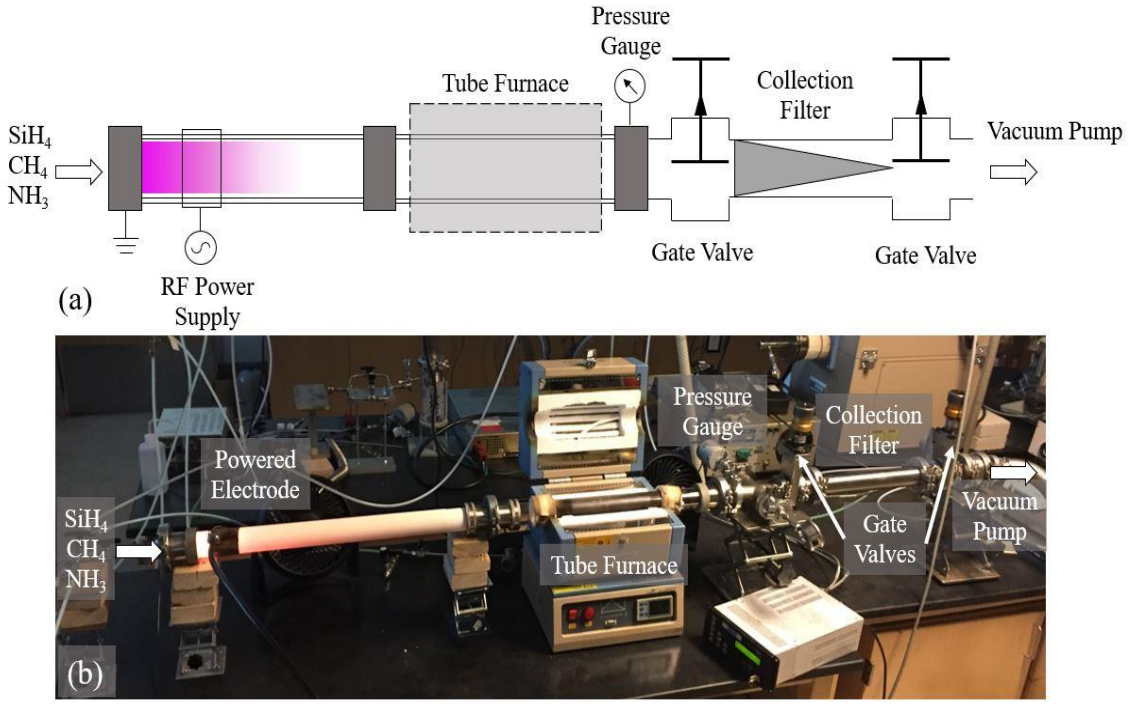

Figure 2.1 (a) Schematic representation of the SiCN non-thermal plasma synthesis reactor with in-flight annealing set up downstream, followed by a pressure control system and stainless-steel filter for capturing nanoparticles. (b) Image of plasma system.

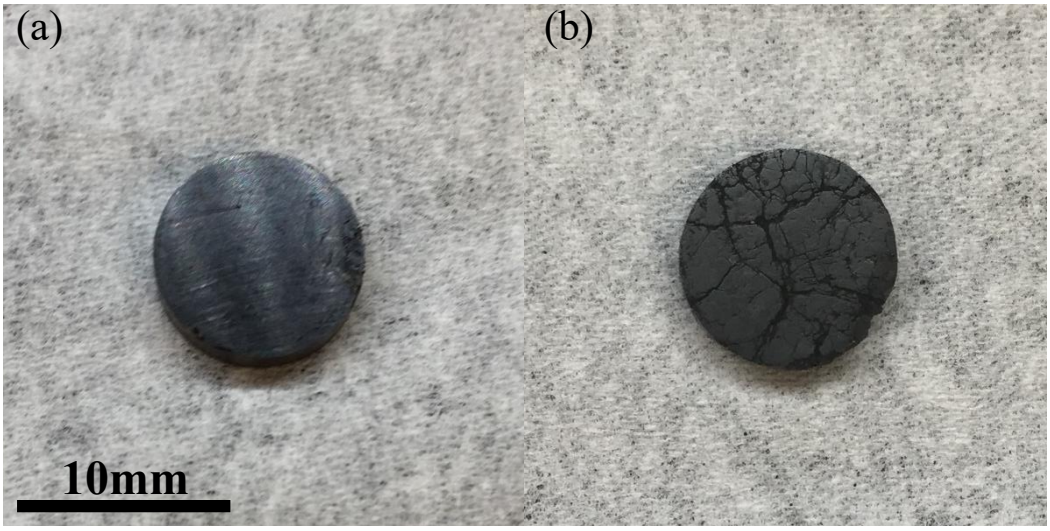

Figure 2.2 Sample 1 (a) with and (b) without in-flight annealing sintered at 1500 °C.

The SiCN nanoparticles were then sintered in a Spark Plasma Sintering (SPS) apparatus (Dr. Sinter-211Lx, Fuji Electronic Industrial, Japan) initially from 1400-1800 °C in steps of 100 °C, as this would completely encompass the range of crystallization temperatures of SiCN mentioned earlier, to determine the thermal stability of the samples. Sample 4 (SiH_4:CH_4:NH_3 flow ratio of approximately 0.8:1:0.8) has additional samples sintered at 1900 °C and 2000 °C since it showed a higher resistance to crystallization. Some works have shown that SPS can create metastable structures in materials due to the high heating rates and short soak times.[31] To ensure that any notable changes in the properties of the amorphous SiCN is not solely due to the sintering

Table 2.1 Parameters for the precursor gas flow rates used to create Samples 1-4. Includes estimated ratios based off precursor flow rate ratio and measured ratios based off of measured atomic percentages with SEM/EDS of samples sintered at 1600 °C.

Sample Name	SiH_4 (sccm)	CH_4 (sccm)	NH_3 (sccm)	CH_4/SiH_4	NH_3/SiH_4	C/Si	N/Si	O/Si
Sample 1	11	10	10	0.91	0.91	0.81±0.01	0.55±0.00	0.21±0.01
Sample 2	8.75	10	10	1.14	1.14	1.25±0.01	0.86±0.01	0.20±0.01
Sample 3	8.75	8	10	0.91	1.14	0.55±0.02	0.66±0.01	0.37±0.04
Sample 4	8.75	10	8	1.14	0.91	1.45±0.08	0.51±0.01	0.24±0.02

process, we sintered Sample 4 at 1600 °C with a soak time of 2 hours, which more closely matches the sintering parameters utilized in studies that use hot-pressing instead of SPS. Samples were prepared for sintering, also in a glovebox to reduce chances of oxidation, by loading the SiCN nanoparticles into 10 mm diameter graphite dies, with graphite foil placed in between the SiCN and punches/die (to protect the graphite tooling and help seal the nanoparticles against oxygen contamination during transfer to the sintering apparatus). The graphite tooling and graphite foil were baked out in the SPS at 600 °C to remove as much moisture as possible from the graphite prior to loading the dies with SiCN. Samples were sintered in a vacuum under 50 MPa of uniaxial pressure with a ramp rate of 150 °C/min and soak at temperature for 30 minutes before cooling down at a rate of 100 °C/min. The temperature of the system was monitored using a pyrometer aimed at the top punch. Prior to characterization, the sintered samples were surface ground to remove the graphite foil and polished to 1μm with diamond polishing media.

X-ray diffraction (XRD) using CuK_{α} radiation (Empyrean Series 2, Malvern PANalytical, UK) was used to confirm whether the SiCN nanoparticles were primarily amorphous prior to sintering and was also used on the sintered samples to determine the sintering temperatures that induce crystallization in the SiCN. Scanning electron microscopy coupled with energy dispersive spectroscopy (SEM/EDS) (NNS450, ThermoFisher Scientific, MA, USA) was used to compositionally map the chemistry of the sintered nanoparticles. Transmission electron microscopy (TEM) (Titan Themis 300, ThermoFisher Scientific, MA, USA) was used to measure the size of the nanoparticles,

and determine the size of any crystalline nanodomains, before and after in-flight annealing. Additionally, TEM/EDS mapping was used on the nanoparticles to confirm the uniform dispersion of carbon and nitrogen, indicating whether the samples are truly SiCN or a SiC/Si_3N_4 composite. Selected area electron diffraction (SAED) was also used on the nanoparticles to confirm any crystalline phases indicated by XRD. X-Ray photoelectron spectroscopy (XPS) (AXIS Ultra DLD, Kratos Analytical, NY, USA) with an Al K_α X-ray source (1486.6 eV) was used on Sample 4, after having been sintering at 1600 °C to observe the bonding structure. Vacuum pressure was kept below 3×10^{-9} torr during acquisition. Ar ion sputtering was carried out at 4 kV for 30 s prior to measurement to remove any oxide layer from the sample. Preliminary mechanical characterization was carried out using a Micro Vicker's Hardness Tester (Model No. 900-391, Phase II, NJ, USA) with a load of 1000 g and a dwell time of 10 seconds for each of the samples sintered at 1600 °C. Density was measured using the Archimedes' Method with propylene glycol as the measuring fluid.

2.4 Results and Discussion

During the initial power sweep using the precursor ratio of Sample 1, it was found that 100 W is the highest power that produces the amorphous SiCN nanoparticles within the test parameters, Figure 2.3a. The materials generated with 110 W and 120 W show XRD peaks at $2\theta = 28.6°$ and 47.4° which are indicative of Si's [111] and [220] peaks,[32] respectively, and the peak at 35° represents the presence of β-SiC [111].[33] As shown in Figure 2.3b. the powder production generally increased with increasing power, but there was a drop in production rate at 120W; this may be the result of an

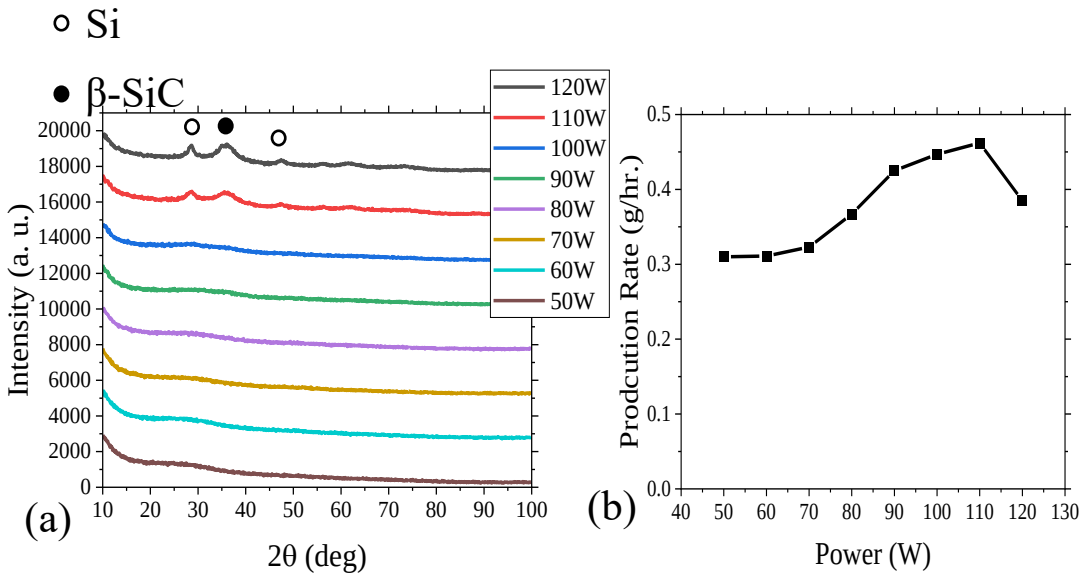

Figure 2.3 a) XRD and b) production rate of Sample 1 SiCN powder produced at power from 50W-120W in steps of 10W.

increase in nanoparticle deposition onto the reactor wall, forming a film at higher powers.[34]

TEM of the nanoparticles in Figure 2.4 shows that the nanoparticles are roughly spherical, ranging in size from 10-50 nm in diameter. Particles are amorphous with crystalline nanodomains, as shown in Figure 2.4a., which are roughly equiaxed and ranging in size from 2-6 nm. Figure 2.4b suggests that after in-flight annealing the crystalline nanodomains grow to approximately 7-14 nm in size, but the majority of the particles remain amorphous. The crystalline nanodomains in Figure 2.4a and 2.4b show silicon based off of the measured d-spacing. SAED of the nanoparticles before in-flight annealing show only diffuse rings with the d-spacing of 3.09 Å, 2.43 Å, and 1.91 Å (Figure 2.4c), in good agreement with spacing of the Si [111], Si [220], and SiC [111]

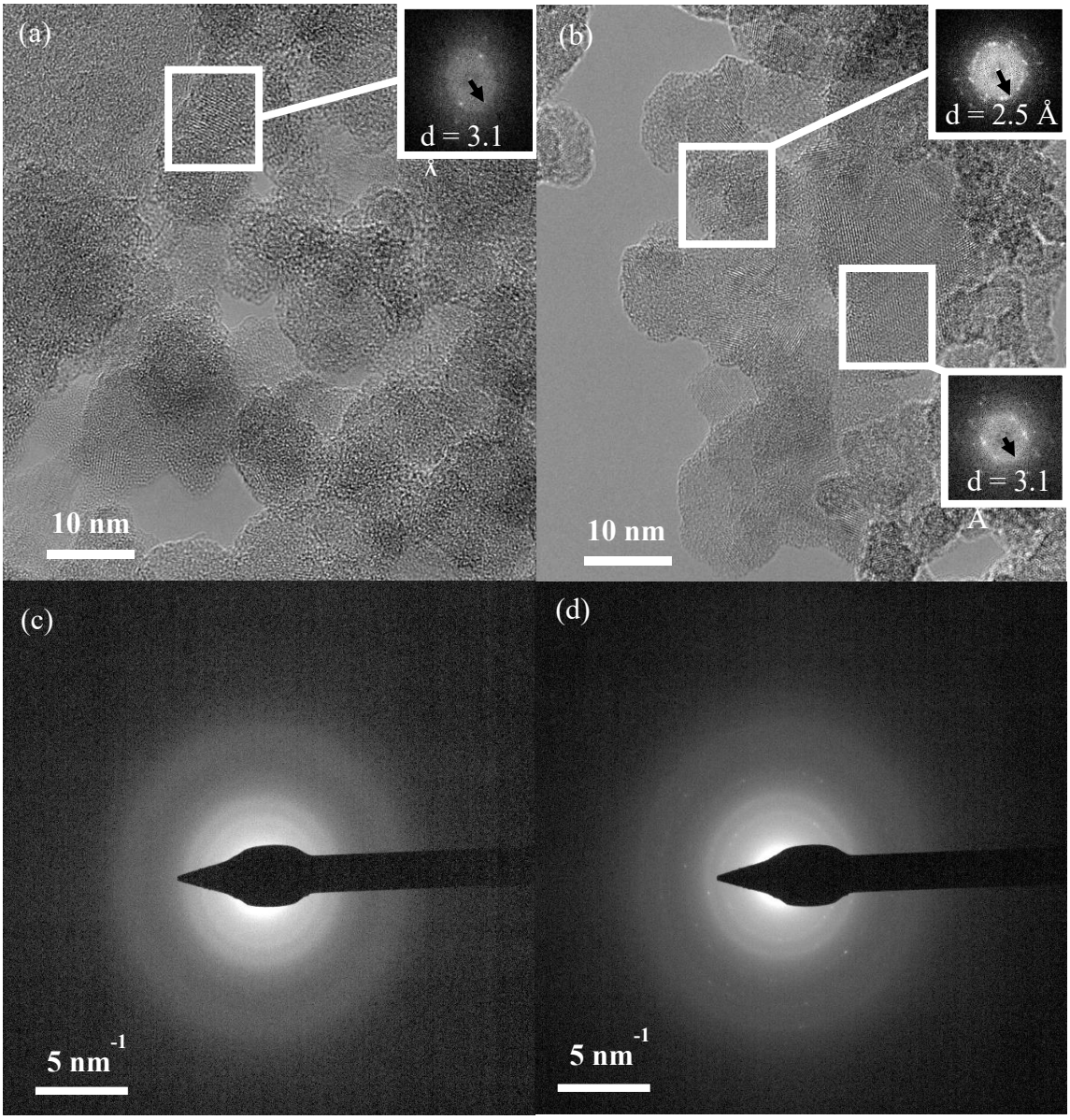

Figure 2.4 Sample 1 SiCN nanoparticles with (a) TEM of nanoparticles without in-flight annealing showing an amorphous matrix with crystalline SiC nanodomains (in the white circles). (b) TEM of nanoparticles with in-flight annealing, resulting in enlarged SiC crystalline nanodomains. (c) SAED of nanoparticles without in-flight annealing showing diffuse Si and SiC rings indicating an amorphous structure. (d) SAED of nanoparticles with in-flight annealing showing the same diffuse Si and SiC rings, but with faint spots representing the larger crystalline nanodomains.

XRD peaks. XRD of the plasma synthesized SiCN nanoparticles with and without in-flight annealing shows little to no difference, with both appearing to be generally amorphous with broad Si and SiC peaks, indicating the presence of crystalline nanodomains within an amorphous matrix, similar to that noted in the work of Wan *et al.*[35] The SAED image after in-flight annealing shows the same diffuse ring, but with some spots within the rings representing the enlarged crystalline nanodomains (Figure 2.4d). Overall, these micrographs confirm that the majority of the material is produced in an amorphous structure, although we observe the occurrence of some crystalline silicon and silicon carbide particles. Most importantly, TEM/EDS shows there is no significant difference in between the distribution of carbon and nitrogen in the samples, as shown in Figure 2.5. This suggests the particles are uniform in chemical composition, with each particle being composed of a uniform mixture of silicon, carbon and nitrogen.

After sintering, XRD shows a high amount of the Si present in Sample 1 (produced at an approximate SiH_4:CH_4:NH_3 ratio of 1:1:1), as seen in Figure 2.6a. For this sample, the Si peaks are present before the appearance of the SiC and Si_3N_4 phases. This behavior suggests that the amorphous SiCN mixture may be oversaturated with Si. This is due to the high ratio of SiH_4 to CH_4 and NH_3 during plasma synthesis. It is also shown that the Sample 1 SiCN undergoes crystallization and segregation into SiC/Si_3N_4 at 1800 °C. Sample 2 is produced at a SiH_4:CH_4:NH_3 ratio of 0.8:1:1, i.e. with less Si compared to Sample 1. It has no Si XRD peaks prior to crystallization of SiC and Si_3N_4, which occurs at 1700 °C (see Figure 2.6b). After crystallization, the relative intensity of the Si peaks versus the SiC and Si_3N_4 peaks is considerably reduced when compared to Sample

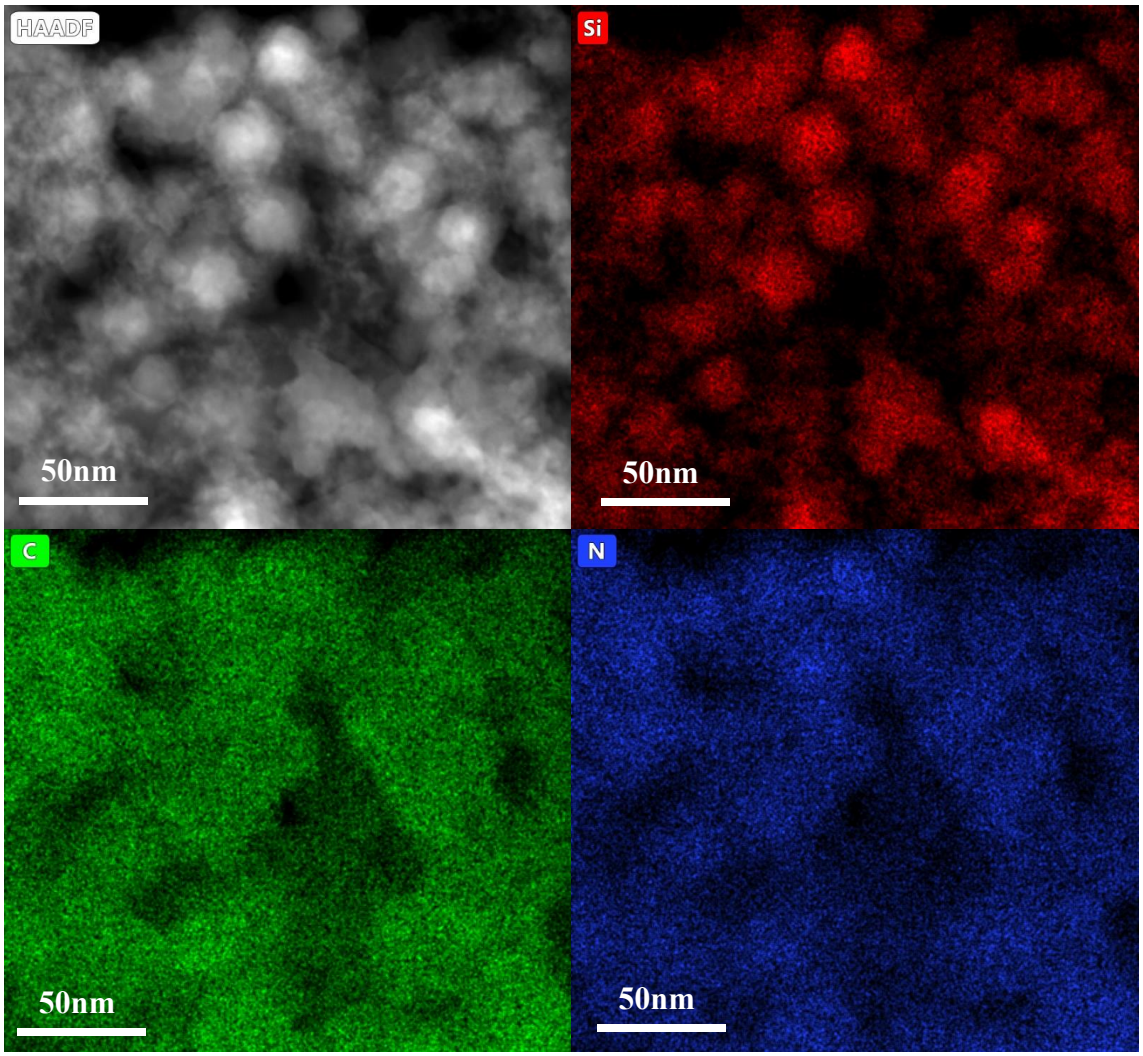

Figure 2.5 TEM/EDS of Sample 1 nanoparticles showing no significant difference in C or N distribution.

1. The C/Si and N/Si ratios have also increased in Sample 2 versus Sample 1 as a result of the reduced Si content, as shown in Table 2.1. Sample 3 with a flow rate ratio of 0.8:0.8:1 and Sample 4 with 0.8:1:0.8, are both similar to Sample 2, but Sample 3 has a reduced methane flow rate while Sample 4 has a reduced ammonia flow rate. This was done to investigate how changes in carbon or nitrogen content within SiCN effects the stability of the solid mixture. Figure 2.6c. and 2.6d, show XRD of Samples 3 (0.8:0.8:1) and Sample 4 (0.8:1:0.8), respectively, which do not crystallize within the initial test

parameters of 1400-1800 °C. Additional, sintering at 1900 °C and 2000 °C of Sample 4 still did not show wide-scale crystallization and segregation, only slight sharpening of SiC peaks, indicating that the SiC crystalline nanodomains are increasing in size. The presence of only SiC peaks is the result of the composition being richer in carbon. Sintering Sample 4 at 1600 °C for 2 hours shows no difference in XRD when compared to the 1600 °C soaked for 30 minutes, implying that the relatively short soak time of SPS was not the cause for the high crystallization temperature observed in the plasma synthesized SiCN.

SEM/EDS measurements are taken to estimate the composition of the SiCN from each sample of nanoparticle feedstock sintered at 1600 °C, as shown in Table 2.1. The changes in compositions of SiCN of the same feedstock, but sintered at different temperatures was relatively similar, with the exception of when Sample 4 feedstock was sintered at 1900 °C and 2000 °C. At 1900 °C and 2000 °C, Sample 4, saw significant drops in N/Si ratios to 0.41 and 0.16, respectively, in comparison to the N/Si ratio of ~0.5, that Sample 4 had from 1400 °C-1800 °C. This is likely nitrogen rapidly outgassing from the SiCN at elevated temperatures. However, when comparing post-sintering compositions between different samples there is a trend similar to the gas flow ratios of the precursors showing that the final composition and be easily controlled through the varying of flow rates of the precursor gases. It should be noted that the oxygen ratio across all the sintered SiCN samples is noticeably high, this could be a result of leaks in the plasma system, impurities in the precursor gases or the cover gas for the glovebox, or remnant moisture in the SPS. However, the two most likely causes are during the transfer

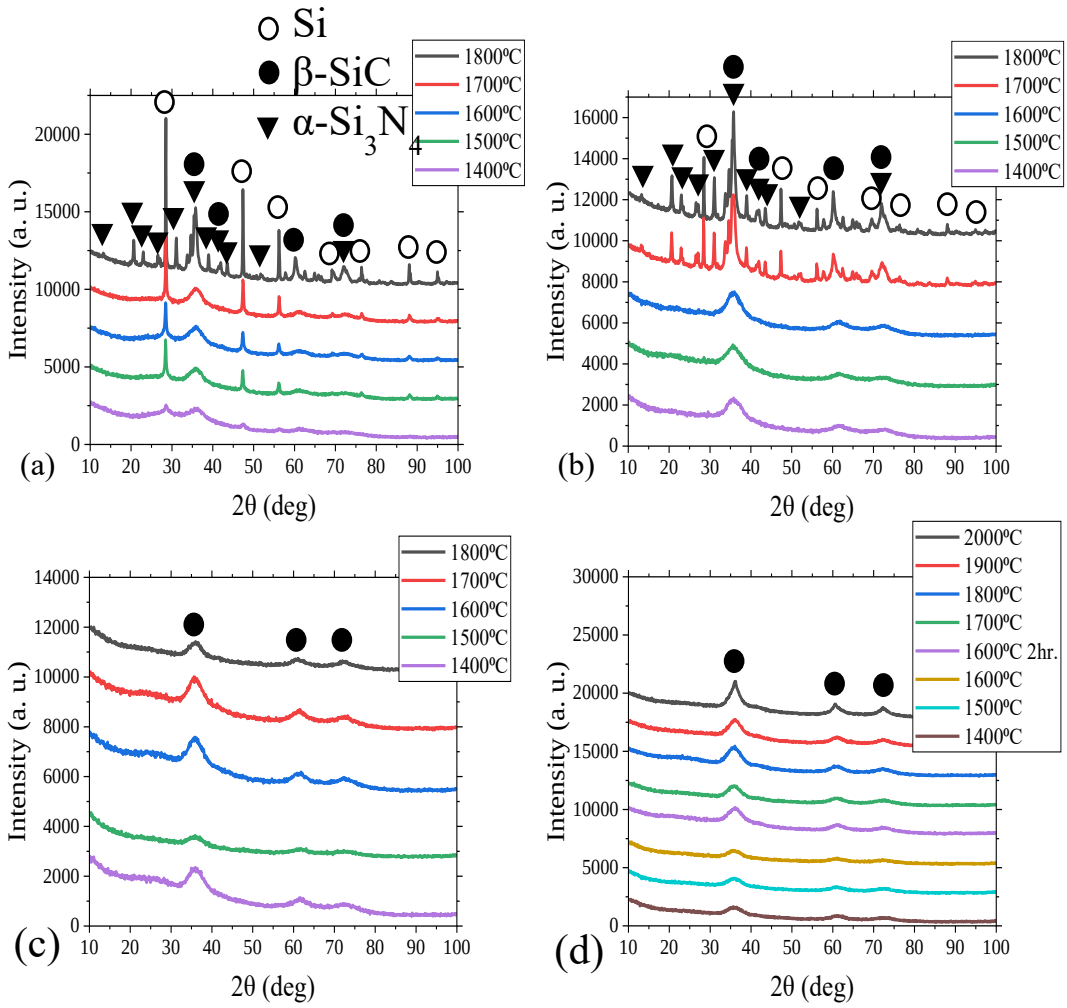

Figure 2.6 a) XRD of Sample 1 sintered from 1400°C-1800°C in steps of 100°C with the amorphous nanoparticles undergoing widespread crystallization and segregation into SiC and Si_3N_4 at 1800°C. Si peaks are present prior to widespread crystallization, possibly due to over saturation of Si in the nanoparticles. b) XRD of Sample 2 lacking the Si peaks of Sample 1 prior to crystallization and a lower crystallization point occurring at 1700°C. c) Sample 3 shows no wide scale crystallization up to 1800°C. d) Sample 4, additionally shows crystallization resistance up to 2000°C, with no noticeable change with regards to soak time.

of the graphite die loaded with SiCN nanoparticles from the glovebox to the SPS, as the graphite foil may not form a perfect seal. The other cause may be after sintering an oxide coating forms on the sintered SiCN samples, and since the sintered samples are porous, can have an oxide layer still within the open pores after polishing and cleaning.

XPS of Sample 4 sintered at 1600 °C is shown in Figure 2.7. The spectrum in Figure 2.7a. represents the Si 2p region which is widely spread from 98 eV to 106 eV. comprising S-C,[36] Si-Si,[37] Si-N and to a lesser extent Si-O bonds.[38] The C 1s spectra in Figure 2.7b. Is centered over the C-C bond, which along with the lack of graphitic carbon peaks seen in XRD in Figure 2.6, means that there is a portion of free amorphous carbon within the SiCN. The presence of C-Si and O=C are at the lower and upper end of the spectra, respectively. There is a possible N-C bond indicating the SiCN is a carbonitride, but it overlaps with the O-C bond.[39] The N 1s spectra is almost entirely comprised of the N-Si bond,[39,40] with a small N-C[41] bond at the upper portion of the spectra, indicating that the plasma synthesized SiCN is a carbonitride. The O 1s spectra in Figure 2.7d. is primarily consisting of the O-Si bond likely from SiO_2,[42] and a small O-C-O bond possibly a small amount of graphene oxide.[43]

It has been reported that polymer-derived SiCN normally crystallize at 1500 °C, but the thermal stability of the amorphous phase can be increased with increasing carbon content, where it is believed that amorphous free carbon acts as a stabilizing factor.[23] SiCN with higher carbon content reported in Mera's work ($SiC_{5.84}N_{1.29}$), crystallized at 1700 °C.[23] The material produced within this work has a carbon content lower than that of Mera's ($SiC_{1.45}N_{0.51}$), yet it exhibits a higher thermal stability (>2000 °C). We

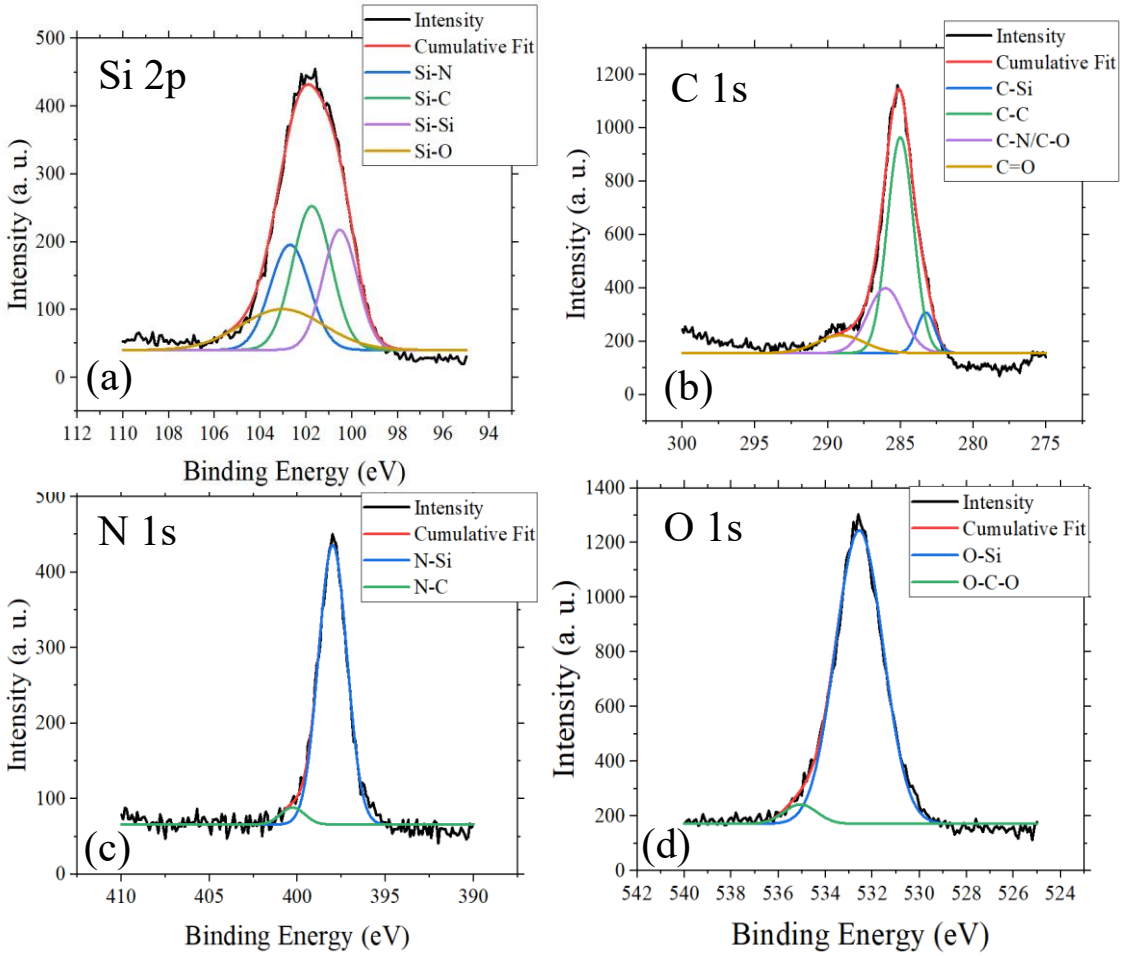

Figure 2.7 XPS data of Sample 4 sintered at 1600 °C for the a) Si 2p peak b) C 1s peak c) N 1s peak and d) O 1s peak.

therefore attribute the higher thermal stability to a more homogeneous mixture of silicon, carbon and nitrogen in the feedstock powder, which is uniquely achievable via low-temperature plasma synthesis.

Overall, these results suggest that the thermal stability of the sintered sample is strongly dependent on composition. They also show that composition can be fine-tuned using the low-temperature plasma synthesis approach. Samples with exceptionally high structural stability have been successfully produced for Si:C:N ratios of 0.8:0.8:1 and 0.8:1:0.8.

One of the goals of this project is to investigate not only the thermal stability, but also the mechanical properties of the sintered SiCN samples. To that end, we have carried out preliminary measurements of their hardness. Unfortunately, at this stage we obtain hardness values that are considerably lower for all the SiCN samples, ranging from 528-637 MPa, than those reported in literature, ranging from 15-26 GPa.[44] This low hardness is likely due to the low density of the samples. We have found that all the produced samples show high porosity at the microscale. SEM of the polished surface of the samples showed areas of incomplete sintering, as shown in Figure 2.8, where particles from the feedstock powder are still distinguishable. The low density may result from outgassing of nitrogen, which is known to occur at temperatures around 1500 °C.[45] One feasible approach to overcome this issue is to sinter at considerably higher pressures compared to what we use here. A high consolidating pressure has been shown to lower

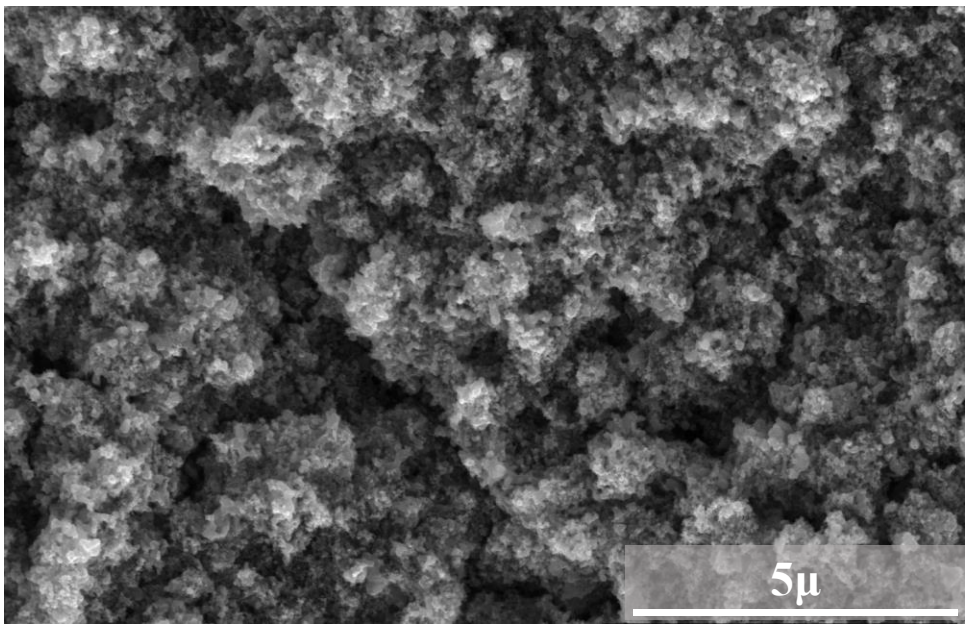

Figure 2.8 SEM of polished surface of Sample 4 sintered at 1600ºC showing a region with incomplete sintering.

the sintering temperatures and to achieve full density without outgassing.[46] At this time, we have not been able to sinter our SiCN feedstock powders at such high pressure, although we expect it would significantly improve the mechanical properties of the sintered materials.

2.5 Conclusions

We have optimized a low-temperature non-thermal plasma process for the production of amorphous silicon carbonitride nanoparticles and used them as feedstock powder for the production of bulk (mm-scale) SiCN samples. We have shown that the composition of the feedstock powder can be controlled precisely by tuning the precursor (SiH_4, CH_4 and NH_3) mixture. Careful TEM analysis shows that Si, C and N are uniformly mixed, with no sign of segregation. We have sintered the feedstock powders via SPS and analyzed the structure of the resulting samples. The precise control of the feedstock powder composition allows optimizing it to maximize thermal stability. Samples produced with a SiH_4:CH_4:NH_3 ratio of 0.8:1:0.8 show no obvious sign of crystallization even when sintered at a temperature of 2000°C, representing a stability improvement of ~500°C when compared to the extant literature. Sintering over an extended period of time (2 hours at 1600°C) also did not result in crystallization. While further optimization of thermomechanical conditions during the sintering step is needed to improve the mechanical properties of the bulk samples, the results here strongly suggest that the low-temperature plasma approach is desirable compared to the more standard use of polymer pyrolysis for the realization of SiCN feedstock powders.

2.6 Citations

[1] J. Goree, *Plasma Sources Sci. Technol.* **1994**, *3*, 400.

[2] U. Kortshagen, U. Bhandarkar, *Phys. Rev. E* **1999**, *60*, 887.

[3] T. Matsoukas, M. Russell, *Journal of Applied Physics* **1995**, *77*, 4285.

[4] A. A. Barragan, S. Hanukovich, K. Bozhilov, S. S. R. K. C. Yamijala, B. M. Wong, P. Christopher, L. Mangolini, *J. Phys. Chem. C* **2019**, *123*, 21796.

[5] A. Ho, R. Mandal, R. R. Lunt, R. J. Anthony, *ACS Appl. Nano Mater.* **2021**, *4*, 5624.

[6] N. B. Uner, E. Thimsen, *J. Phys. D: Appl. Phys.* **2019**, *53*, 095201.

[7] D. Coleman, T. Lopez, O. Yasar-Inceoglu, L. Mangolini, *J. Appl. Phys.* **2015**, *117*, 193301.

[8] D. Coleman, L. Mangolini, *ACS Omega* **2019**, *4*, 10089.

[9] S. Askari, A. U. Haq, M. Macias-Montero, I. Levchenko, F. Yu, W. Zhou, K. (Ken) Ostrikov, P. Maguire, V. Svrcek, D. Mariotti, *Nanoscale* **2016**, *8*, 17141.

[10] F. Xu, G. Nava, P. Biswas, I. Dulalia, H. Wang, Z. Alibay, M. Gale, D. J. Kline, B. Wagner, L. Mangolini, M. R. Zachariah, *Chemical Engineering Journal* **2022**, *430*, 133140.

[11] N. J. Kramer, R. J. Anthony, M. Mamunuru, E. S. Aydil, U. R. Kortshagen, *J. Phys. D: Appl. Phys.* **2014**, *47*, 075202.

[12] P. Xia, E. K. Raulerson, D. Coleman, C. S. Gerke, L. Mangolini, M. L. Tang, S. T. Roberts, *Nat. Chem.* **2020**, *12*, 137.

[13] P. Xia, J. Schwan, T. W. Dugger, L. Mangolini, M. L. Tang, *Advanced Optical Materials* **2021**, *9*, 2100453.

[14] J. Schwan, K. Wang, M. Lee Tang, L. Mangolini, *Nanoscale* **2022**, *14*, 17385.

[15] S. A. Hosseini, D. Coleman, S. Bux, P. A. Greaney, L. Mangolini, *Phys. Rev. Mater.* **2022**, *6*, 075401.

[16] A. Alvarez Barragan, N. V. Ilawe, L. Zhong, B. M. Wong, L. Mangolini, *J. Phys. Chem. C* **2017**, *121*, 2316.

[17] S. Exarhos, A. Alvarez-Barragan, E. Aytan, A. A. Balandin, L. Mangolini, *ACS Energy Lett.* **2018**, *3*, 2349.

[18] L. Bharadwaj, Y. Fan, L. Zhang, D. Jiang, L. An, *Journal of the American Ceramic Society* **2004**, *87*, 483.

[19] L. An, R. Riedel, C. Konetschny, H.-J. Kleebe, R. Raj, *Journal of the American Ceramic Society* **1998**, *81*, 1349.

[20] R. Riedel, H.-J. Kleebe, H. Schönfelder, F. Aldinger, *Nature* **1995**, *374*, 526.

[21] R. Raj, *Journal of the American Ceramic Society* **1993**, *76*, 2147.

[22] R. M. Morcos, G. Mera, A. Navrotsky, T. Varga, R. Riedel, F. Poli, K. Müller, *Journal of the American Ceramic Society* **2008**, *91*, 3349.

[23] G. Mera, R. Riedel, F. Poli, K. Müller, *Journal of the European Ceramic Society* **2009**, *29*, 2873.

[24] P. Colombo, G. Mera, R. Riedel, G. D. Sorarù, *Journal of the American Ceramic Society* **2010**, *93*, 1805.

[25] D. Galusek, F. L. Riley, R. Riedel, *Journal of the American Ceramic Society* **2001**, *84*, 1164.

[26] S. E. Pratsinis, S. Vemury, *Powder Technology* **1996**, *88*, 267.

[27] R. Dez, F. Ténégal, C. Reynaud, M. Mayne, X. Armand, N. Herlin-Boime, *Journal of the European Ceramic Society* **2002**, *22*, 2969.

[28] S. Y. Kim, D. K. Choi, D.-H. Yeo, H. S. Shin, H. G. Yoon, *Journal of the European Ceramic Society* **2020**, *40*, 5349.

[29] R. D'Amato, M. Falconieri, S. Gagliardi, E. Popovici, E. Serra, G. Terranova, E. Borsella, *Journal of Analytical and Applied Pyrolysis* **2013**, *104*, 461.

[30] T. Lopez, L. Mangolini, *Nanoscale* **2014**, *6*, 1286.

[31] J. Suffner, M. Lattemann, H. Hahn, L. Giebeler, C. Hess, I. G. Cano, S. Dosta, J. M. Guilemany, C. Musa, A. M. Locci, R. Licheri, R. Orrú, G. Cao, *Journal of the American Ceramic Society* **2010**, *93*, 2864.

[32] T. D. Hatchard, J. R. Dahn, *J. Electrochem. Soc.* **2004**, *151*, A838.

[33] H.-J. Kleebe, D. Suttor, H. Müller, G. Ziegler, *Journal of the American Ceramic Society* **1998**, *81*, 2971.

[34] Y. Ding, R. Yamada, R. Gresback, S. Zhou, X. Pi, T. Nozaki, *J. Phys. D: Appl. Phys.* **2014**, *47*, 485202.

[35] J. Wan, M. J. Gasch, C. E. Lesher, A. K. Mukherjee, *Journal of the American Ceramic Society* **2003**, *86*, 857.

[36] S. Contarini, S. P. Howlett, C. Rizzo, B. A. De Angelis, *Applied Surface Science* **1991**, *51*, 177.

[37] A. R. Chourasia, *Surface Science Spectra* **2001**, *8*, 45.

[38] G.-R. Yang, Y.-P. Zhao, Y. Z. Hu, T. Paul Chow, R. J. Gutmann, *Thin Solid Films* **1998**, *333*, 219.

[39] E. Vassallo, A. Cremona, F. Ghezzi, F. Dellera, L. Laguardia, G. Ambrosone, U. Coscia, *Applied Surface Science* **2006**, *252*, 7993.

[40] Y. Awad, M. A. El Khakani, C. Aktik, J. Mouine, N. Camiré, M. Lessard, M. Scarlete, H. A. Al-Abadleh, R. Smirani, *Surface and Coatings Technology* **2009**, *204*, 539.

[41] Z.-W. Deng, R. Souda, *Diamond and Related Materials* **2002**, *11*, 1676.

[42] J. Finster, D. Schulze, F. Bechstedt, A. Meisel, *Surface Science* **1985**, *152–153*, 1063.

[43] R. Al-Gaashani, A. Najjar, Y. Zakaria, S. Mansour, M. A. Atieh, *Ceramics International* **2019**, *45*, 14439.

[44] S. R. Shah, R. Raj, *Acta Materialia* **2002**, *50*, 4093.

[45] C. Haluschka, C. Engel, R. Riedel, *Journal of the European Ceramic Society* **2000**, *20*, 1365.

[46] M. J. Gasch, J. Wan, A. K. Mukherjee, *Scripta Materialia* **2001**, *45*, 1063.

Chapter 3. Spark Plasma Sintering of Non-Thermal Plasma Synthesized Silicon Carbonitride Nanoparticles

3.1 Abstract

Amorphous silicon carbonitride (SiCN) has significant potential as a high-temperature structural material, however, current reports on its synthesis suggest a lack of methods to limit its devitrification into crystalline phases. In this work, non-thermal plasma synthesis and high-pressure spark plasma sintering (SPS) are used to produce bulk, dense SiCN samples. An applied uniaxial pressure of 500 MPa with a soak temperature at 1600 °C produced SiCN with a Vickers hardness up to 16.1 GPa, fracture toughness of 2.6 MPa·$m^{1/2}$, and Young's Modulus up to 247 GPa. XRD and DSC showed that SiCN stayed primarily amorphous through the sintering process; however, some SiC nanocrystalline domains formed within the amorphous matrix. Electron microscopy shows a lack of pores, but with pockets of the Y_2O_3 dispersed among the SiCN. Archimedes' measurements of samples sintered at 1400 °C and 1600 °C determined the density of the samples to be 3.02 and 3.21 g/cm^3, respectively. The results suggest the potential for using amorphous plasma, synthesized nanoparticles and spark plasma sintering to produce bulk amorphous or composite ceramic materials with novel stoichiometry and properties.

3.2 Introduction

Amorphous silicon carbonitride (SiCN) has demonstrated promise for future high-temperature applications such as turbine blades and thermal barrier coatings. In addition to good room temperature mechanical properties for an engineering ceramic such as high

hardness,[1-3] amorphous SiCN possesses excellent oxidation resistance and creep resistance at temperatures up to 1300 °C.[5,7] Meanwhile, traditional engineering ceramics such as SiC and Si_3N_4 begin to volatize and oxidize above 1200 °C, converting these materials into mechanically weaker SiO_2. Creep causes cavitation at these temperatures as well, which drives crack formation and propagation.[4] Studies by An *et al.* have shown amorphous SiCN to have a steady-state creep rate too small to be effectively measured at 1280 °C,[5] contrasting with the creep behavior of commonly used engineering ceramics. For example, Si_3N_4 has been reported to have a steady state strain rate of approximately 10^{-8} s^{-1} under similar testing conditions.[6] Raj *et al.* have measured amorphous SiCN to have a parabolic rate constant for oxidation as 1.1×10^{-18} to 3.8×10^{-18} m^2/s at 1350 °C in ambient air and notes that this oxidation behavior is significantly lower than sintered SiC and Si_3N_4 reported from other literature.[7]

SiCN is commonly produced through polymer pyrolysis, whereby polymer pre-ceramics such as polysilanes and polycarbosilanes undergo shaping, cross-linking, and pyrolysis.[8] However, this process results in an open porous material due to outgassing byproducts such as hydrogen and hydrocarbons preventing pore closure.[9] An alternative method to achieve full density SiCN is through pulverization of pyrolyzed, porous SiCN into a powder through ball milling, followed by sintering through hot pressing or spark plasma sintering (SPS) to densify the powder into bulk. However, ball milling has been known to introduce contaminants into the milled materials.[10] In excessive amounts, impurities can negatively impact the structural properties of SiCN by forming mechanically weaker phases. In addition, it is challenging to produce fully

densified amorphous SiCN as the sintering temperature and crystallization temperature are both nominally 1500 °C, at which point amorphous SiCN precipitates into a crystalline SiC/Si_3N_4 nanocomposite.[11] As a result, most published works that engage in sintering SiCN are in actuality making SiC/Si_3N_4 composites.[3,12-15]

Recently, our group has described an alternative path towards the fabrication of amorphous SiCN that circumvents some of these issues. This involves the production of SiCN nanopowders through non-thermal plasma synthesis.[16] In short, gaseous precursors are used to produce contaminant-free amorphous SiCN nanopowders in a continuous process. In addition, it was shown that varying the gas flow rate ratios of the precursors controlled the composition of the SiCN, including what phases were present after thermal treatment. This led to an amorphous SiCN phase with an increased resistance to crystallization at temperatures exceeding 2000 °C. Attempts at sintering of the plasma-synthesized SiCN nanopowders were unsuccessful due to the outgassing of N_2 at 1500 °C. We have found that this inhibits sintering, leading to poor mechanical performance.

Two general approaches to overcome the outgassing problem have been tested. One method is to sinter in a pressurized atmosphere of N_2 (1-5 bar) to suppress the outgassing of N_2 from the SiCN.[20] The other method is to use high pressure sintering, where a uniaxial pressure ranging from a few hundred MPa to 1 GPa is applied during sintering to engage early onset sintering.[13] The latter approach reduces the temperature needed to achieve full density to below the outgassing temperature of N_2 of 1500°C. In this work, we explore the high-pressure spark plasma sintering of non-thermal plasma

synthesized amorphous SiCN nanoparticles at 500 MPa and 1600 °C with goal of fully densifying non-thermal plasma synthesized amorphous SiCN without complete devitrification. We then compare the mechanical properties of the resultant compacts with those reported in the literature for other bulk synthesis approaches.

3.3 Methods & Materials

SiCN nanoparticles were produced through non-thermal plasma synthesis using gaseous precursors with the following flow rates: SiH_4+Ar (1.37% SiH_4) at 640 sccm, CH_4 at 10 sccm, and NH_3 at 8 sccm. The design of the system (Figure 1a.) was based on previous work.[16] Non-thermal plasmas are versatile systems for the production of nanoparticles,[17] with recent reports confirming that they are good sources of ceramic-based nanomaterials as well.[18,19] The first stage contains a capacitively coupled plasma generated using a radio frequency (13.56 MHz) power supply. The second stage consists of an MTI OTF-1200X tube furnace where the nanoparticles are passed through to remove excess hydrogen.[21] An in-flight annealing stage is important; without it, excess hydrogen on the surface of the SiCN nanoparticles outgasses during sintering and becomes trapped in pores, impeding sintering. The plasma is run at a power of 100 W at a pressure of 3 torr, while the tube furnace is set to 1000 °C. The nanoparticles (Figure 1b.) were collected on a stainless-steel mesh filter placed after the tube furnace. To prevent oxygen contamination of the SiCN, the filter with nanoparticles was pressurized to atmospheric pressure with argon before being sealed and transferred to an argon glovebox. While in the glovebox, the nanoparticles are extracted from the filter and mixed with a 15 wt% Y_2O_3 sintering aid in a tumbler overnight. The Y_2O_3 induces liquid

phase sintering, where the sintering aid melts and flows in between the particles. Part of the solid SiCN particles go into solution in the Y_2O_3 melt, forming an oxynitride liquid phase. This creates a solution-precipitation process with faster interparticle diffusion compared to the evaporation-condensation process that occurs when no sintering aids are used.[12,22] However, the Y_2O_3 was observed to stay in the material after sintering and the relatively low melting point in comparison to SiCN reduces the mechanical performance at high temperatures.

Spark plasma sintering of the SiCN nanoparticles was carried out with a Fuji Electronic Industrial SPS-515. For each sample, 0.1 g of the SiCN nanoparticles were pressed into a 5 mm diameter high pressure sintering punch and die set consisting of graphite and SiC components, the design of which is shown in Figure 1c. Nominal

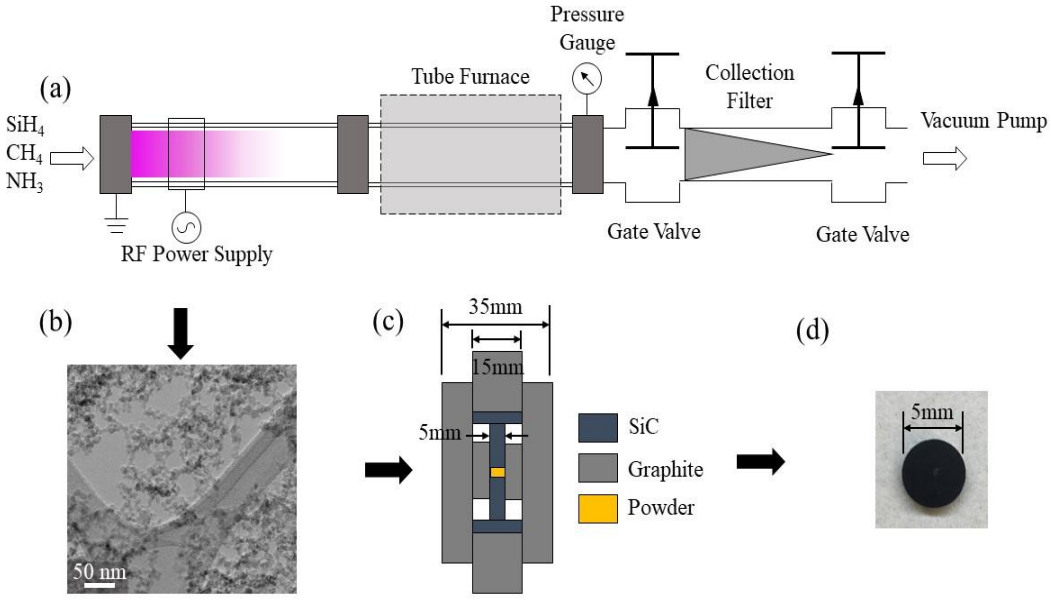

Figure 3.1 (a) Schematic of non-thermal plasma synthesis system. (b) TEM of collected SiCN nanoparticles. (c) Schematic of the high pressure SiC+graphite punch and die setup used to sinter amorphous SiCN nanoparticles under 500 MPa of pressure. (d) Sintered SiCN disk.

temperature is measured using a pyrometer aimed at the top outer punch. The temperature of the inner die during sintering is estimated to be approximately 200 °C colder than the point the pyrometer measures. The estimation was determined by a dry run up to 1000 °C comparing the readings of the pyrometer aimed at the top outer punch and thermocouple inserted through a hole in the outer die and in contact with the inner die, with the temperature offset extrapolated to the target temperatures. Subsequently, all reported temperatures are of the estimated inner die temperature. The samples were sintered under vacuum at 1400 °C and 1600 °C, with a heating rate of 150 °C/min, soaked at temperature for 30 min, and cooled at a rate of 100 °C/min. During sintering, the samples were initially held at 600 °C (the lower limit of the pyrometer) under minimal applied pressure to allow remnant hydrogen still on the SiCN nanoparticles to outgas before pore closure at higher temperatures, the regular ramp rate up to the soak temperature was continued once the SPS chamber pressure returned to its initial state (~3Pa), signaling that the outgassing has stopped. The SiCN powders are densified under 500 MPa of uniaxial pressure applied once the soak temperature is reached. After sintering, the SiCN are black, crack-free disks (Figure 1d).

After sintering, samples are extracted from the die, mounted in epoxy, and polished to 1 μm finish with diamond lapping pads. The samples are then characterized with X-Ray diffraction (XRD) performed on a Malvern PANalytical Empyrean Series 2 with a CuK_{α} source to detect crystalline phases that may form during sintering. A ThermoFisher Scientific NNS450 Scanning Electron Microscope (SEM) is used with Energy Dispersive X-Ray Spectroscopy (EDS) to observe the microstructure and

determine the extent of phase segregation during sintering. The bulk density of the sintered SiCN samples is measured using the Archimedes' Method with propylene glycol as the submersion media.

Differential scanning calorimetry (DSC) was used to determine what reactions were occurring during sintering. A SiCN sample was scanned in a Netzsch DSC 404 F3 Pegasus to determine the crystallization temperature. The SiCN samples were placed in an Al_2O_3 crucible with a disk of graphite foil in between the sample and the crucible to prevent a reaction between the two. A run under the same conditions was undertaken with just the graphite foil and the crucibles to establish a background which was subsequently corrected for in the scan with SiCN. A ramp rate of 10 °C/min and a hold at 1550 °C for 10 min under an Ar atmosphere was used. The sample was scanned several times as the initial scan detected a continuous endothermic trend throughout the entire temperature range, obscuring the crystallization peaks at higher temperatures, this was likely caused by remnant hydrogen outgassing.

Nanoindentation studies were performed on a Bruker Ti950 Triboindenter equipped with a NanoDMA III low-force transducer at a rate of 600 hz with a maximum load of 10 mN, a loading rate of 400 μN/s, and a diamond Berkovich indenter to measure hardness, H, and reduced elastic modulus, E_r. The indenter was calibrated on fused quartz (FQ) according to best practices for indenter correction and machine compliance, while the tip area function (TAF) was calibrated on indents ranging from 0.1-10 mN in polished 5N-pure Aluminum and allowing for varying power-law fitting constants to better account for low-load, low-displacement indentation behavior, following best practices for

low-depth indentation with regards to calibration of system and indenter compliance. For all indentations, a quasi-static trapezoidal loading profile with 5 s loading/unloading periods and a 2 s quasi-static was followed, allowing for varying strain rate and depth by varying load. Four indentation tests were conducted for the SiCN samples sintered at 1400 °C and 1600 °C, comprising of 1) a varying load indentation line from 1-10 mN to establish system compliance and drift characteristics, and 2-4) grids of indents comprising of at least 30 individual indents per set space at equidistant points on the cross-section; in all cases, indents were spaced at least 10 μm apart minimize overlap of indentation stress fields.

For grid indentations, a peak load of 4 mN was identified as the local minima for thermal/compliance drift and optimal fitting to FQ calibrated indentation range (38-198 nm) (Figure 2). Routine compliance checks throughout testing and sequences of cleaning and then profiling of the Berkovich indenter tip were conducted regularly throughout testing, as tip blunting throughout testing can result in insufficient plastic deformation observed during periodic calibration standards at the indentation depths of interest. Thus, calibration checks on system compliance and transducer performance were conducted daily, and the calculated radius of curvature for the indenter tip was recorded due to tip blunting caused by repeated indentation of materials with $H > 20$ GPa. Hardness (H) reported here was (h_c), the tip-area function corrected hardness, derived from the projected area, while the Elastic modulus reported from the experimental study was E_r, the (substrate-effect-corrected) reduced elastic modulus; each defined respectively defined by the Oliver-Pharr[23] method as:

$$E_r = \frac{\sqrt{\pi}}{2}\frac{S}{A} \quad (1)$$

which relates the reduced elastic modulus, E_r, to the projected contact area A, and calculated stiffness, $S = dP / dh$.

$$H = \frac{P_{max}}{A} \quad (2)$$

where A is the projected area of contact at peak load, P_{max}

$$P(h) = \alpha\,(h - h_f)^m \quad (3)$$

where P is the load, hf is the total elastic displacement of the indenter tip during a complete cycle of loading/unloading, and α and m are constants derived from fitting unloading-section behavior to a power function of the form. Fracture toughness was estimated using the indentation fracture method reported on by Anstis *et al*.[24]

$$Kc = 0.016\left(\frac{E_r}{H_v}\right)^{0.5}\left(\frac{P_v}{c^{1.5}}\right) \quad (4)$$

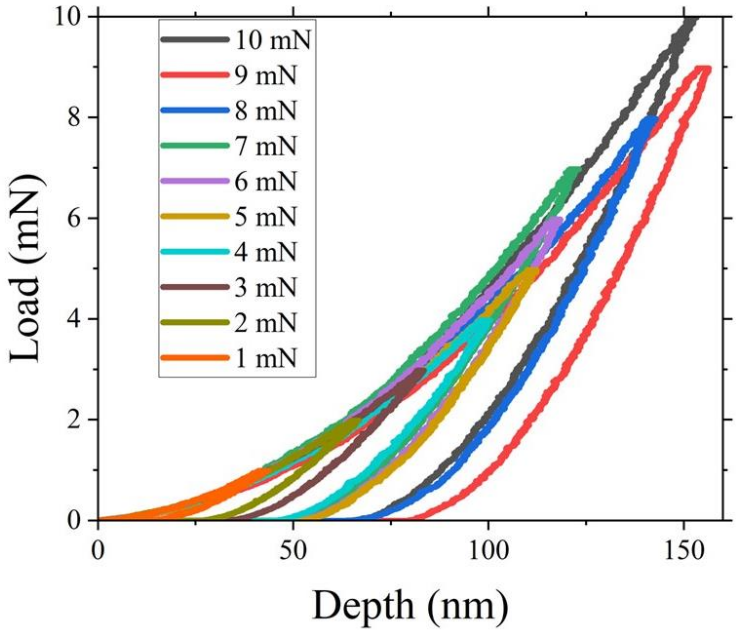

Figure 3.2 Loading/unloading curves with peak loads from 1mN to 10mN of SiCN sintered at 1400°C.

Where K_c is the fracture toughness, H_v is Vickers hardness, P_v is the indentation load, and c is the radial crack length. The Vickers hardness was measured with a Phase II Micro Vickers Hardness Tester, Model No. 900-390 with a load of 1000 g and a dwell time of 10 sec with a minimum of 10 measurements per sample.

3.4 Results and Discussion

The X-ray diffraction pattern (Figure 3a.) of plasma synthesized SiCN nanoparticles shows them to be primarily amorphous, with no discernible peaks other than a very shallow peak at 2θ = 36°, which is β-SiC's [111] lattice plane,[25] indicating the presence of some crystalline nanodomains. After sintering the SiCN at 1400 °C and 1600 °C the [111] peak sharpened and β-SiC's secondary lattice planes are now present at 2θ = 60° for [222] and 2θ = 72° for [311]. For the 1600 °C sample, α-Si_3N_4 and β-Si_3N_4 are present while the β-SiC peaks sharpen as a sign of continued crystallization at higher temperatures. α-Si_3N_4 has been reported in literature to be the first nitride phase to precipitate out of amorphous SiCN,[12,26] and upon reaching 1500 °C α-Si_3N_4 begins to irreversibly convert to β-Si_3N_4.[27] However, the presence of peaks from both Si_3N_4 phases in the XRD pattern indicates that the α-β transition has not completed, likely due to the relatively short sintering times of SPS and the low atomic diffusivity of Si_3N_4. Further exploration of the reactions during sintering was probed via DSC of the prebaked SiCN nanoparticles (Figure 3b). At 1275 °C an exothermic trend begins, peaking at 1350 °C representing the crystallization of the SiCN into SiC/Si_3N_4 immediately followed by an endothermic rise past the baseline representing N outgassing.

Electron microscopy studies were undertaken to observe the microstructure for particle bonding, morphology, and phase separation. SEM images of the SiCN sintered at 1400 °C showed noticeably lighter regions throughout the sample, which will be shown to be unintegrated Y_2O_3 sintering aid (Figure 4a). Higher magnification of the sample also indicated incomplete sintering, as clusters of unsintered nanoparticles are prevalent throughout the sample (Figure 4b). Chemical measurements via EDS show the sintered bulk SiCN to have a composition of $SiC_{0.86}N_{0.65}$ and indicates the light regions mentioned before contains high concentration of Y (pink) and O (cyan) (e.g. the Y_2O_3 sintering aid) (Figure 4e). SEM images of the SiCN processed at the higher temperature of 1600 °C did not show the same Y_2O_3 concentrated spots as the 1400 °C sample, but instead shows darker regions dispersed among lighter regions (Figure 4c). Additionally, higher magnification SEM imaging of the 1600 °C sample does not show nanoparticle clusters such as the ones present in the lower temperature sample, signaling a higher order of densification (Figure 4d). These observations point to the fact that 1400 °C, even under 500MPa, is not enough to completely sinter the SiCN nanoparticles. For the sample sintered at 1600 °C, EDS measured the composition to be $SiC_{0.76}N_{0.58}$ similar to the 1400 °C sample, although a slight reduction in N due to outgassing at the higher sintering temperature. The EDS measurement also shows the lighter regions to contain a slightly higher concentration of Y_2O_3 than the surrounding darker regions (Figure 4f), meaning

the higher temperature allows for the sintering aid to more effectively dissolve and go into solution with the SiCN.

The mechanical properties of the sintered SiCN at 1400 °C and 1600 °C, as well as comparative data from literature, are shown in Table 3.1. The samples' Vickers hardness was measured to be 14.5 GPa and 16.1 GPa for 1400 °C and 1600 °C, respectively, within the same hardness range as other reported fully densified SiCN in literature. The lower hardness for the lower temperature sample is attributed to the incomplete densification, as discussed previously. In comparison to a similar study using SPS on plasma synthesized SiCN nanoparticles, but with a lower sinter pressure of 50 MPa which reported a maximum hardness of 1.2 GPa,[16] the increased pressure of 500 MPa shows a significant improvement on densification and the resulting mechanical properties. Young's modulus was measured to be 235 GPa and 247 GPA for the 1400 °C

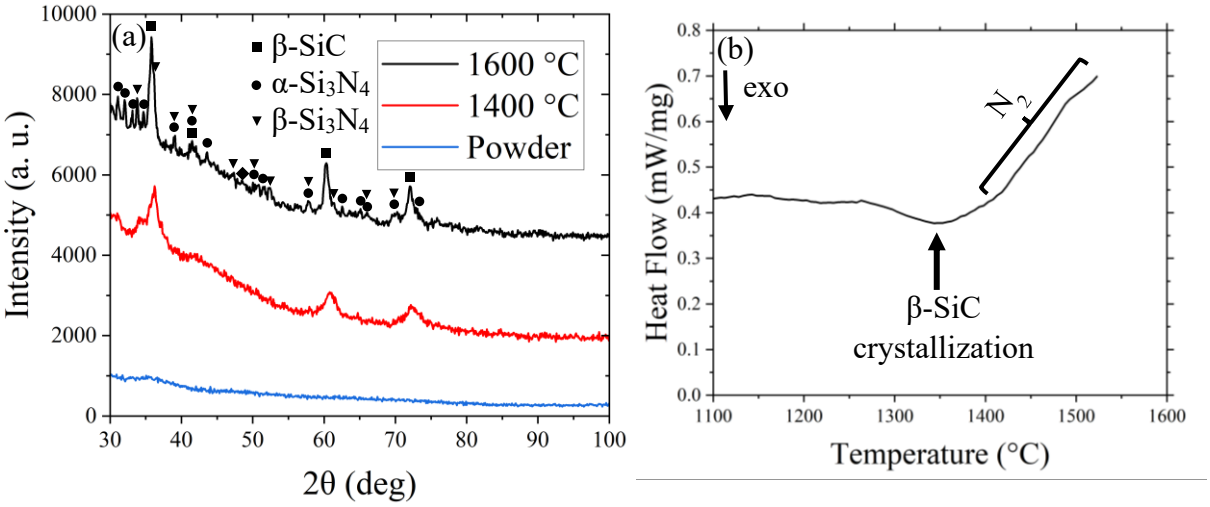

Figure 3.3 (a) XRD of SiCN nanoparticles before sintering and after sintering at 1400 °C and 1600 °C and SiC peaks (b) DSC of SiCN where SiC starts to crystallize at 1400 °C followed by outgassing of N_2.

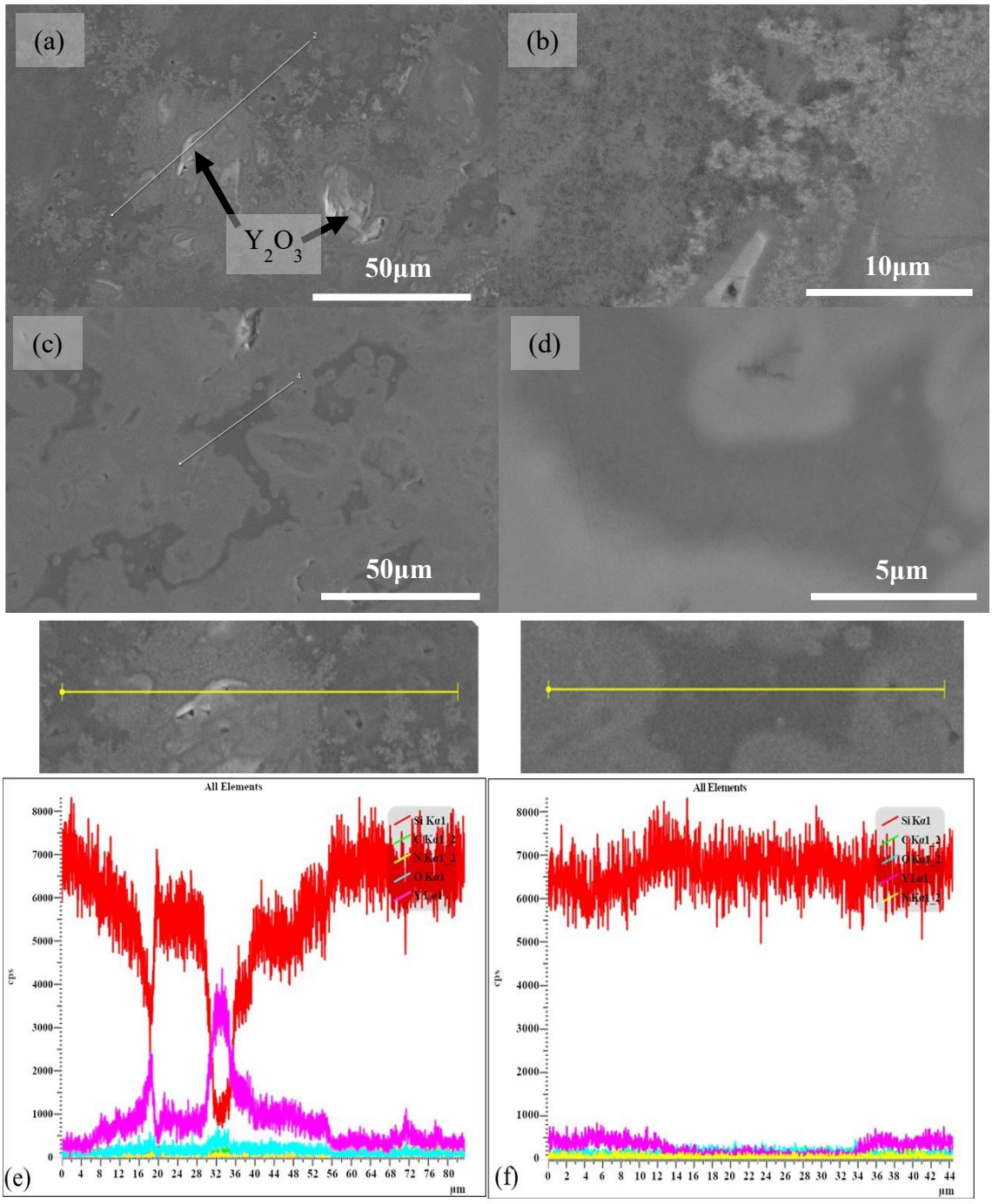

Figure 3.4 SEM images of SiCN sintered at 1400 °C (a) (b) and 1600 °C (c) (d). (e) EDS linescan of the 1400 °C sample shows the presence of unincorporated Y_2O_3 sintering aid likely left over as a combination of too low of a sintering temperature for too short of a time. (f) EDS linescan of the 1600 °C sample has better dispersion of the Y_2O_3, although a slight difference is still present in different regions.

and 1600 °C samples, respectively. Applying the measured Young's modulus to Equation (4), the fracture toughness was calculated to be 2.5 MPa·$m^{1/2}$ and 2.6 MPa·$m^{1/2}$, equivalent to SiCN in other works, also shown in Table 3.1. The density was measured for the 1400 °C and 1600 °C samples to be 3.02 and 3.21 g/cm^3, respectively. This is higher than the reported measured density of amorphous SiCN of 2.33 g/cm^3,[1,2] and is more in line with the density of crystalline SiC and Si_3N_4 of 3.2 g/cm^3.[14] While some crystallization is shown in XRD, the density could be interpreted to mean that complete crystallization occurred in the 1600 °C sample, possibly as crystalline nanodomains as to explain the broad peaks. As mentioned before, Figure 3a. shows the 1400 °C sample contains a mixture of amorphous SiCN and nanocrystalline β-SiC, which explains its

Table 3.1 Room temperature mechanical properties of amorphous SiCN produced through multiple methods

Sample Name	Method	Vickers Hardness (GPa)	Fracture Toughness (MPa·$m^{1/2}$)	Young's Modulus (GPa)	Density (g/cm^3)	Reference
A	Warm Press (1000°C)	25	1.1	150	2.3	[1]
B	Pyrolysis (1100°C)	13	--	121	2.32	[2]
C	Pyrolysis (1050°C)	--	2.5	183	2.1	[28]
D	Pyrolysis (1050°C)	6.7	2.1	105	1.95	[29]
E	CVD†	13	--	136	--	[30]
F	Magnetron Sputtering†	18.9	--	241	--	[31]
H	SPS (1400°C, 500MPa)	14.5	2.5	235	3.02	this work
I	SPS (1600°C, 500MPa)	16.1	2.6	247	3.21	this work

†Amorphous SiCN nano-film

density exceeding that of amorphous SiCN. Wan *et al.* also reported a higher-than-expected density of 2.87 g/cm^3 and 2.92 g/cm^3 when sintering amorphous SiCN under 2 GPa at 1400 °C and 1600 °C, respectively.[12] With the 1400 °C sample being a mixture of amorphous and crystalline phases and the 1600 °C sample being completely crystalline. Overall, the high-pressure sintering proved effective at consolidating plasma synthesized SiCN nanoparticles, due to the lower temperatures where N_2 outgassing has less of an impact on densification, as well as the increased pressure counteracting pore growth from trapped gasses.

3.5 Conclusions

We have sintered plasma-synthesize SiCN nanoparticle to near full density using high-pressure SPS. The application of 500 MPa as opposed to a previous study that used 50 MPa provided a significant increase in density and, by extension, the mechanical properties. This brought hardness and fracture toughness up to 16.1 MPa and 2.6 MPa·m$^{1/2}$, respectively, as well as a Young's Modulus of 247 MPa in line with other studies on the bulk properties of SiCN. During sintering, partial to complete crystallization occurred, based on sintering temperature. DSC additionally shows a crystallization event occurring prior to the sintering temperatures at 1350 °C, this is associated with the formation of crystalline SiC. The comparable mechanical properties of sintered plasma-synthesized SiCN with its sintered polymer-derived counterpart demonstrates the viability for low-temperature plasma synthesis coupled with SPS for creating structural materials.

3.6 Citations

[1] Shah SR, Raj R. *Acta Materialia*. **2002**,50(16):4093.

[2] Galusek D, Riley FL, Riedel R. *Journal of the American Ceramic Society*. **2001**,84(5):1164–1166.

[3] Haluschka C, Kleebe H-J, Franke R, Riedel R. *Journal of the European Ceramic Society*. **2000**,20(9):1355–1364.

[4] Raj R. *Journal of the American Ceramic Society*. **1993**,76(9):2147–2174.

[5] An L, Riedel R, Konetschny C, Kleebe H-J, Raj R. *Journal of the American Ceramic Society*. **1998**,81(5):1349–1352.

[6] Nixon RD, Koester DA, Chevacharoenkul S, Davis RF. *Composites Science and Technology*. **1990**;37(1):313–328.

[7] Raj R, An L, Shah S, Riedel R, Fasel C, Kleebe H-J. *Journal of the American Ceramic Society*. **2001**, 84(8):1803–1810.

[8] Colombo P, Mera G, Riedel R, Sorarù GD. *Journal of the American Ceramic Society*. **2010**, 93(7):1805–1837.

[9] Konetschny C, Galusek D, Reschke S, Fasel C, Riedel R. *Journal of the European Ceramic Society*. **1999**, 19(16):2789–2796.

[10] Kim SY, Choi DK, Yeo D-H, Shin HS, Yoon HG. *Journal of the European Ceramic Society*. **2020**, 40(15):5349–5356.

[11] Iwamoto Y, Völger W, Kroke E, Riedel R, Saitou T, Matsunaga K. *Journal of the American Ceramic Society*. **2001**, 84(10):2170–2178.

[12] Wan J, Gasch MJ, Lesher CE, Mukherjee AK. *Journal of the American Ceramic Society*. **2003**, 86(5):857–863.

[13] Gasch MJ, Wan J, Mukherjee AK. *Scripta Materialia*. **2001**, 45(9):1063–1068.

[14] Degenhardt U, Stegner F, Liebscher C, *et al. Journal of the European Ceramic Society*. **2012**, 32(9):1893–1899.

[15] Wan J, Duan R-G, Mukherjee AK. *Scripta Materialia*. **2005**, 53(6):663–667.

[16] Herzberg S, Mathaudhu SN, Mangolini L. *Plasma Processes and Polymers*. **2023**, 20(8):e2300021.

[17] Kortshagen UR, Sankaran RM, Pereira RN, Girshick SL, Wu JJ, Aydil ES. *Chem Rev*. **2016**, 116(18):11061–11127.

[18] Coleman D, Lopez T, Yasar-Inceoglu O, Mangolini L. *Journal of Applied Physics*. **2015**, 117(19):193301.

[19] Exarhos S, Alvarez-Barragan A, Aytan E, Balandin AA, Mangolini L *ACS Energy Lett*. **2018**, 3(10):2349–2356.

[20] Friess M, Bill J, Golczewski J, *et al. Journal of the American Ceramic Society*. **2002**, 85(10):2587–2589.

[21] Lopez T, Mangolini L. *Nanoscale*. **2014**, 6(3):1286–1294.

[22] German RM. In: German RM, ed. *Sintering: from Empirical Observations to Scientific Principles*. Boston: Butterworth-Heinemann, **2014**:247–303.

[23] Oliver WC, Pharr GM. *Journal of Materials Research*. **1992**, 7(6):1564–1583.

[24] Anstis G r., Chantikul P, Lawn B r., Marshall D b. *Journal of the American Ceramic Society*. **1981**, 64(9):533–538.

[25] Ortiz AL, Sánchez-Bajo F, Cumbrera FL, Guiberteau F. *Materials Letters*. **2001**, 49(2):137–145.

[26] Kleebe H-J, Suttor D, Müller H, Ziegler G. *Journal of the American Ceramic Society*. **1998**, 81(11):2971–2977.

[27] Messier DR, Riley FL, Brook RJ. *J Mater Sci*. **1978**, 13(6):1199–1205.

[28] Bauer A, Christ M, Zimmermann A, Aldinger F. *Journal of the American Ceramic Society*. **2001**, 84(10):2203–2207.

[29] Nishimura T, Haug R, Bill J, Thurn G, Aldinger F. *Journal of Materials Science*. **1998**, 33(21):5237–5241.

[30] Awad Y, El Khakani MA, Aktik C, *et al. Surface and Coatings Technology*. **2009**, 204(4):539–545.

[31] Ctvrtlik R, Al-Haik MS, Kulikovsky V. *J Mater Sci*. **2015**, 50(4):1553–1564.

Chapter 4. Conclusions

This work has undertaken the exploration of combining low-temperature non-thermal plasma synthesis with SPS to create and characterize non-equilibrium materials in bulk form. Using the gaseous precursors SiH_4, CH_4, and NH_3, amorphous SiCN nanoparticles were created. Through the variation of the flow rate ratios of the precursor gasses, different compositions of SiCN were created, each showing different degrees of thermal stability for the amorphous phase up to 2000 °C. The presence of C-N bonds does show that the SiCN is in fact a true carbonitride, as opposed to only amorphous SiC/Si_3N_4. In addition, C-C bonds are present as well, a sign of amorphous carbon. Measures have not yet been taken to quantify the ratio of each amorphous phase within the nanoparticles. Initial attempts at consolidation of the SiCN nanoparticles into bulk form were unsuccessful due to N_2 outgassing above 1500 °C. The low relative density resulted in low mechanical properties well below results reported in literature.

Additional attempts at sintering using high pressure tooling and a uniaxial pressure of 500 MPa proved sufficient to lower the sintering temperature, reducing N_2 outgassing. These higher-pressure samples showed improved mechanical properties on par with literature. The density of these samples in combination with XRD and DSC indicate crystallization occurs before 1400 °C and increases up to complete crystallization at 1600 °C.

Overall, non-thermal plasma synthesis is demonstrated to be capable of making non-equilibrium materials with bulk properties equivalent to traditional methods of production for the associated material. Non-thermal plasma synthesis has a versatility in

creating contaminate free nanoparticles with either amorphous or crystalline structures from a plethora of gaseous or liquid precursors. Giving it the potential to expand into the creation and study of many different types of non-equilibrium ceramics and metals in future works.